EXPLORING VOLCANIC AND INDUSTRIAL GEOHAZARDS USING DENSE GEOPHONE ARRAYS AND SEISMIC INTERFEROMETRY

by
Santiago Emilio Rábade Garcia

A dissertation submitted to the faculty of
The University of Utah
in partial fulfillment of the requirements for the degree of

Doctor of Philosophy
in
Geophysics

Department of Geology and Geophysics
The University of Utah
May, 2024

The University of Utah Graduate School

STATEMENT OF DISSERTATION APPROVAL

The dissertation of **Santiago Emilio Rabade Garcia**

has been approved by the following supervisory committee members:

Fan-Chi Lin , Chair Date Approved

Kristine Louise Pankow , Member Date Approved

Jamie Mark Farrell , Member Date Approved

Keith David Koper , Member Date Approved

Carl Tape , Member Date Approved

and by **William P. Johnson** , Chair of

the Department of **Geology and Geophysics**

and by Darryl P. Butt, Dean of The Graduate School.

ABSTRACT

This dissertation explores the geohazards of volcanic and industrial systems using ambient noise cross-correlations and nodal stations. The main goal is to better understand the systems as a snapshot in time or through temporal evolution. This is achieved using the cross-correlation of ambient noise to enhance subtle signals that contain information regarding the crustal structure or the seismic source of the system. To study the systems statically, we measure phase velocity of Rayleigh and Love waves using slant stacking or single beamforming and Rayleigh wave ellipticity. Then, we can jointly invert these measurements to leverage the different sensitivities. We also studied a system dynamically by back projecting the energy emitted by the system to understand the variations through time.

We first study the top 16 km of the crust in south-central Alaska using more than 300 seismic stations. We determine the Rayleigh wave phase velocity and ellipticity from ambient noise cross-correlation using single beamforming. We perform an MCMC joint inversion to better understand the Denali Volcanic Gap, the Denali Fault, and the overall crustal structure of the Alaska Suture Zone.

Secondly, we study the shallow crustal structure of the Lower East Rift Zone of the Kilauea Volcano in Hawaii Big Island. We compute the Love and Rayleigh phase velocity and the Rayleigh wave ellipticity. The results offer a glimpse into the dike system and the different intrusions.

Third, we use the seismic signals emitted by a longwall coal mine to understand the mining activity and its evolution through time. We use ambient noise cross-correlation and the correlation coefficient to separate the background noise from the mining activity. Then we locate the mining activity throughout the time of recording at 5-minute and 24-hour

resolution to catch the advance of the longwall and the extraction activity. The comparisons with the seismicity show promise on the proposed workflow.

The success of these projects show the potential of using ambient noise interferometry to study natural or industrial system to better understand the geohazards.

TABLE OF CONTENTS

CHAPTER 1

INTRODUCTION

The Earth is a dynamic planet, constantly undergoing processes that shape its surface and impact human activity. Among these processes, geohazards such as volcanic eruptions and industrial activities pose significant risks to human life and infrastructure. Understanding these geohazards is paramount for mitigating their potential impact and ensuring the safety and well-being of communities worldwide.

Studying the geohazards of natural or industrial systems is crucial for risk assessment, disaster preparedness, and hazard mitigation efforts. Scientists and policymakers can develop effective strategies to minimize their impact and protect vulnerable populations by understanding the underlying processes driving these systems.

Passive and active seismic interferometry has proved to be a valuable and flexible tool to map the shallow crust, including small structures like fault zones (Mordret et al., 2019; Wang, Allam, et al., 2019; Gkogkas et al., 2021), as well as complex hydrothermal features (Wu et al., 2017, 2019, 2021). Furthermore, extracting extra information from the surface waves, like Rayleigh wave ellipticity (Lin et al., 2014; Berg et al, 2018, 2020), has proved to be a tool to improve the constraint on the crustal structure and the quality of the shear wave inversion. This methodological advancement, coupled with the technological progress in the instrumentation of portable nodal seismometers (Karplus and Schmandt, 2018), makes mapping small and complex structures feasible.

To reduce the geohazards from natural and industrial systems we study them statically dynamically in Chapter 2 (i.e. spatiotemporal variations) and statically in Chapter 3 and 4 (i.e. the crustal structure). In this work I explore the use of both approaches to study two volcanic systems statically (Rabade et al., 2023) and one industrial system dynamically (Rabade et al, 2022).

In Chapter 2, we propose a workflow to study the spatiotemporal evolution of the seismic sources of a longwall coal mine. Using ambient noise cross-correlation on data collected from a 17-geophone array, we separated the mining operations from the background noise using the similarity of waveforms. Then, we located the signals that correlated with the longwall location and the seismicity of the mine.

In Chapter 3, we used a temporal array of 306 geophones deployed in the winter of 2019, complemented with regional broadband stations to map the shallow- to mid-crust of South-Central Alaska across the Alaska Range. We measured Rayleigh wave phase velocity and ellipticity for 4 to 12 s using single beamforming/slant stacking. We obtained the shear wave model of the top 16 km using a Markov chain Monte Carlo joint inversion. We observe a low-velocity zone beneath the Denali Volcanic, probably related to the accumulation of magmatic material from the slab. We identify the Denali Fault as a narrow, vertical, low-velocity zone extending to 12 km deep. In the shallow, we mapped the Susitna and Tanana sedimentary basins.

In Chapter 4, we build upon the approach used in our Alaska research to map the Lower East Rift Zone dike of Kilauea volcano in the Big Island of Hawaii. Using data from a temporal deployment in 2019 and the island network, we measured Love and Rayleigh phase velocity and Rayleigh wave ellipticity. We observe higher velocity at the 1955 fissures track and lower velocities north of the 2018 estimated dike location. On a larger scale, we observe that the northern part of the area of study is faster than the southern area.

1.1 References

Berg, E.M., Lin, F.C., Allam, A., Qiu, H., Shen, W. and Ben-Zion, Y., 2018. Tomography of Southern California via Bayesian joint inversion of Rayleigh wave ellipticity and phase velocity from ambient noise cross-correlations. Journal of Geophysical Research: Solid Earth, 123(11), pp.9933-9949.

Berg, E.M., Lin, F.C., Allam, A., Schulte-Pelkum, V., Ward, K.M. and Shen, W., 2020. Shear velocity model of Alaska via joint inversion of Rayleigh wave ellipticity, phase velocities, and receiver functions across the Alaska Transportable Array. Journal of Geophysical Research: Solid Earth, 125(2), p.e2019JB018582.

Gkogkas, K., F. C. Lin, A. A. Allam, and Y. Wang, 2021, Shallow damage zone structure of the wasatch fault in Salt Lake City from ambient-noise double beamforming with a temporary linear array, Seismol. Res. Lett., 92, no. 4, 2453–2463, doi: 10.1785/0220200404.

Karplus, M., and B. Schmandt, 2018, Preface to the focus section on Geophone Array Seismology, Seismol. Res. Lett., 89, no. 5, 1597–1600, doi: 10.1785/0220180212.

Mordret, A., P. Roux, P. Boué, and Y. Ben-Zion, 2019, Shallow three-dimensional structure of the San Jacinto fault zone revealed from ambient noise imaging with a dense seismic array, Geophys. J. Int., 216, no. 2, 896–905, doi: 10.1093/gji/ggy464.

Lin, F.C., Tsai, V.C. and Schmandt, B., 2014. 3-D crustal structure of the western United States: application of Rayleigh-wave ellipticity extracted from noise cross-correlations. Geophysical Journal International, 198(2), pp.656-670

Rabade, S., Lin, F.C., Tape, C., Ward, K.M., Waldien, T. and Allam, A., 2023. The crustal magmatic structure beneath the Denali Volcanic Gap imaged by a dense linear seismic array. Journal of Geophysical Research: Solid Earth, 128(12), p.e2023JB027152.

Rabade, S., Wu, S.M., Lin, F.C. and Chambers, D.J., 2022. Isolating and Tracking Noise Sources across an Active Longwall Mine Using Seismic Interferometry. *Bulletin of the Seismological Society of America*, *112*(5), pp.2396-2407.

Wang, Y., A. Allam, and F. C. Lin, 2019, Imaging the Fault Damage Zone of the San Jacinto Fault Near Anza With Ambient Noise Tomography Using a Dense Nodal Array, Geophys. Res. Lett., 46, no. 22, 12938–12948, doi: 10.1029/2019GL084835.

Wu, S. M., F. C. Lin, J. Farrell, and A. Allam, 2019, Imaging the Deep Subsurface Plumbing of Old Faithful Geyser From Low-Frequency Hydrothermal Tremor Migration, Geophys. Res. Lett., 46, no. 13, 7315–7322, doi: 10.1029/2018GL081771.

Wu, S. M., F. C. Lin, J. Farrell, W. E. Keller, E. B. White, and J. D. G. Hungerford, 2021, Imaging the Subsurface Plumbing Complex of Steamboat Geyser and Cistern Spring With Hydrothermal Tremor Migration Using Seismic Interferometry, J. Geophys. Res. Solid Earth, 126, no. 4, doi: 10.1029/2020JB021128.

Wu, S. M., F. C. Lin, J. Farrell, B. Shiro, L. Karlstrom, P. Okubo, and K. Koper, 2020, Spatiotemporal Seismic Structure Variations Associated With the 2018 Kīlauea Eruption Based on Temporary Dense Geophone Arrays, Geophys. Res. Lett., 47, no. 9, 1–10, doi: 10.1029/2019GL086668.

Wu, S. M., K. M. Ward, J. Farrell, F. C. Lin, M. Karplus, and R. B. Smith, 2017, Anatomy of Old Faithful From Subsurface Seismic Imaging of the Yellowstone Upper Geyser Basin, Geophys. Res. Lett., 44, no. 20, 10,240-10,247, doi: 10.1002/2017GL075255.

CHAPTER 2

ISOLATING AND TRACKING NOISE SOURCES ACROSS AN ACTIVE LONGWALL MINE USING SEISMIC INTERFEROMETRY

Rabade, S., Wu, S. M., Lin, F. C., & Chambers, D. J. (2022). Isolating and Tracking Noise Sources across an Active Longwall Mine Using Seismic Interferometry. *Bulletin of the Seismological Society of America*, 112(5), 2396-2407. ©Owned by the authors, published by Bulletin of the Seismological Society of America, 2022. With kind permission of the Seismological Society of America.

Isolating and Tracking Noise Sources across an Active Longwall Mine Using Seismic Interferometry

Santiago Rabade*[1], Sin-Mei Wu[1,2], Fan-Chi Lin[1], and Derrick J. A. Chambers[3]

ABSTRACT

The ability to monitor seismicity and structural integrity of a mine using seismic noise can have great implication for detecting and managing ground-control hazards. The noise wavefield, however, is complicated by induced seismicity and heavy machinery associated with mining operations. In this study, we investigate the nature of time-dependent noise cross-correlations functions (CCFs) across an active underground longwall coal mine. We analyze one month of continuous data recorded by a surface 17 geophone array with an average station spacing of ∼200 m. To extract coherent seismic signals, we calculate CCFs between all stations for each 5-min window. Close inspection of all 5-min CCFs reveals waveforms that can be categorically separated into two groups, one with strong and coherent 1–5 Hz signals and one without. Using a reference station pair, we statistically isolate time windows within each group based on the correlation coefficient between each 5-min CCF and the monthly stacked CCF. The daily stacked CCFs associated with a high correlation coefficient show a clear temporal variation that is consistent with the progression of mining activity. In contrast, the daily stacked CCFs associated with a low correlation coefficient remain stationary throughout the recording period in line with the expected persistent background noise. To further understand the nature of the high correlation coefficient CCFs, we perform 2D and 3D back projection to determine and track the dominant noise source location. Excellent agreement is observed on both short (5-min) and long (daily) time scales between the CCF determined source locations, the overall migration of the active mining operation, and cataloged seismic event locations. The workflow presented in this study demonstrates an effective way to identify and track mining induced signals, in which CCFs associated with background noise can be isolated and used for further temporal structural integrity investigation.

KEY POINTS

- Isolating the mining activity from background noise is important for passive seismic monitoring.
- We show that seismic interferometry can be used to identify and track mining activity in a longwall mine.
- Our proposed framework can lead to simultaneous monitoring of subsurface seismicity and structure changes.

Supplemental Material

INTRODUCTION

A better understanding of the temporal seismicity migration and structural change in a mining setting is important for hazard mitigation. Traditional seismic passive monitoring focuses on determining the seismic event distribution and source characteristics using observed energetic seismic phases (Eaton, 2018). In the case of underground mines, such a method meets a variety of objectives, including documenting seismicity, ground motion monitoring, back analysis of significant failures, assessing mine design performance, monitoring kinematics of geological structures, and rockburst hazard management (Mendecki *et al.*, 2010; Swanson *et al.*, 2016; Nordström *et al.*, 2020). A similar approach has also been widely applied in other industrial applications, including hydraulic fracturing (Maxwell *et al.*, 2012), CO_2 and water injection (Verdon *et al.*, 2010), enhanced

---

[1] Department of Geology and Geophysics, University of Utah, Salt Lake City, Utah, U.S.A., https://orcid.org/0000-0003-1750-489X (SR); https://orcid.org/0000-0001-8330-471X (S-MW); https://orcid.org/0000-0003-0394-6830 (F-CL); [2] Swiss Seismological Service, ETH Zürich, Zurich, Switzerland; [3] National Institute for Occupational Safety and Health, Spokane, Washington, D.C., U.S.A., https://orcid.org/0000-0003-3656-6607 (DJAC)

*Corresponding author: san.rabade@utah.edu

Cite this article as Rabade, S., S.-M. Wu, F.-C. Lin, and D. J. A. Chambers (2022). Isolating and Tracking Noise Sources across an Active Longwall Mine Using Seismic Interferometry, *Bull. Seismol. Soc. Am.* **XX**, 1–12, doi: 10.1785/0120220031

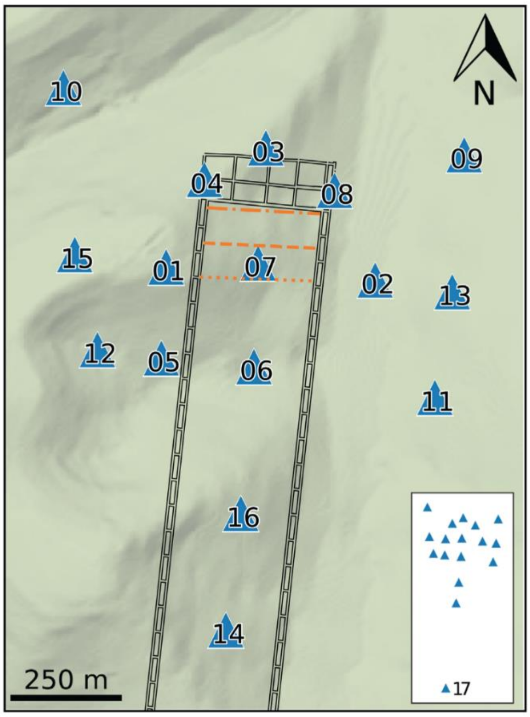

Figure 1. Station location (triangles), and longwall location for days 7/09, 7/16, and 7/26 marked as dash-dotted, dashed, and dotted line, respectively. The solid lines depict the mine structure. The inset shows the full array configuration including one further station. The color version of this figure is available only in the electronic edition.

geothermal systems (Majer *et al.*, 2007), tunnel development (Chen *et al.*, 2011), and several others. Such an approach, however, has some drawbacks. First, it depends on the presence of seismicity, meaning less-active mines (or mining areas) receive no benefit from monitoring and aseismic processes are undetectable. Second, industrial noise associated with mining can severely limit the monitoring system's sensitivity. Third, although automated processing of seismicity is improving, often significant time is required by human analysts to produce high-quality event catalogs.

Seismic interferometry, on the other hand, offers an alternative way to identify changes in seismic source characteristics and structural properties by detecting weaker but coherent seismic signals. A handful of recent works in a mining setting have demonstrated the potential applications of seismic interferometry in underground mine settings. Dales *et al.* (2017a,b) showed seismic interferometry can be used to locate impulsive and persistent sources within mines. They performed synthetic tests and located individual events using seismic waveforms recorded within the mine, obtaining high temporal resolution using impulsive sources. Czarny *et al.* (2016) used two surface broadband stations several kilometers apart to detect subtle velocity decreases associated with longwall mining and induced seismicity. Lu and Feng (2017) used the conveyor belt as a source to image changes in the mining face.

Outside of mining, studies have also demonstrated noise cross-correlation functions (CCF), in addition to studying the velocity structure by extracting the empirical Green's function (Lobkis and Weaver, 2001; Shapiro *et al.*, 2005; Lin *et al.*, 2008; Nicolson *et al.*, 2014; Spica *et al.*, 2016), can be used to understand the seismic source when transient or persistent noise sources are present (Haney, 2010, 2014; Cros *et al.*, 2011; Ballmer *et al.*, 2013; Wu *et al.*, 2017, 2019, 2021). These applications focus on the extraction of coherent wavefields emitted by the spurious seismic source, which can be used to study the source property (e.g., location) based on the associated time arrivals, amplitudes, and polarizations in the CCFs. Early continental-scale studies have located persistent sources of longer-period surface waves, including the 26 s microseism energy from Gulf of Guinea (Shapiro *et al.*, 2006) and the Kyushu microseism (Zheng *et al.*, 2011). It has also been used to study and find more localized hydrothermal and volcanic tremor activities in Yellowstone (Cros *et al.*, 2011; Wu *et al.*, 2019, 2021), Alaska (Haney, 2010, 2014), Hawaii (Ballmer *et al.*, 2013), and Iceland (Li *et al.*, 2017). Moreover, by exploring the stability of the noise correlation coda signals, temporal structural variation can be also inferred (Brenguier *et al.*, 2008; Clements and Denolle, 2018; Wu *et al.*, 2020). Using seismic interferometry to study temporal source and structure variation in a mine setting nevertheless has not been fully explored.

In this study, we investigate the possibility of using temporal variation of CCFs to resolve changes in source location and velocity structure across an active longwall coal mine. Longwall mining is a method of underground mining that allows the extraction of full slices or panels of mineral resources (Fig. 1). The mining machines consist of one or more shearers or ploughs (cutting instruments) mounted on a series of self-advancing hydraulic ceiling supports. The most common mechanism of the seismicity is a normal fault with a near-vertical plane parallel to the mining wall (Stec, 2007; Bischoff *et al.*, 2010; Sen *et al.*, 2013; Verdon *et al.*, 2018). In addition, the longwall coal seismicity also includes events with non-double-couple sources related to roof caving and events with orientations associated with tectonic features or preexisting faults.

By analyzing data from a 17-station seismic geophone array (Fig. 1) above an active longwall coal mine, we first exploit the use of seismic interferometry to characterize and isolate time windows with different noise properties (i.e., dominated by background noise versus mining induced seismicity). We then migrate the CCF waveforms that contain mining-related seismic energy to obtain the 2D/3D source location using consecutive 24 hr and 5-min time windows throughout the deployment time periods. For both time scales, our results

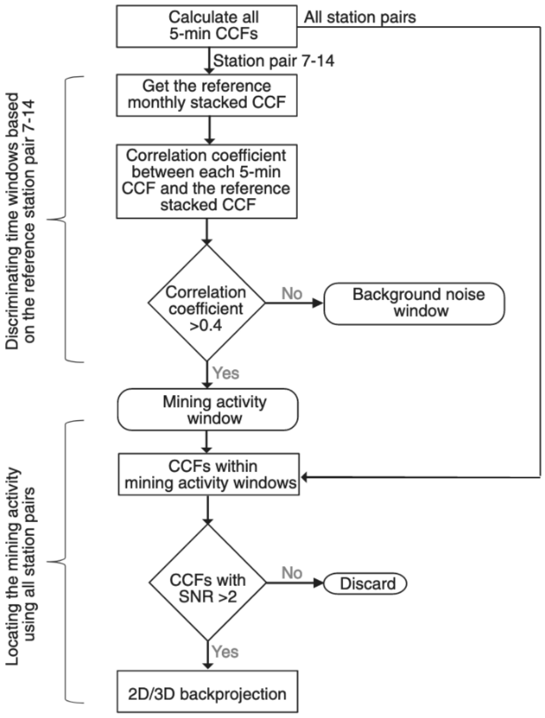

Figure 2. The workflow for the analyses applied in this study.

agree with the position of the overall mining longwall and the cataloged seismicity location. We demonstrate that this workflow (Fig. 2) can be used to monitor seismic activity in complex settings with continuous data recorded on the surface and show how periods of mining-dominated noise can be distinguished from quieter times, which may be useful for structural imaging and monitoring.

DATA

We deployed 17 three-component (3C) autonomous 5 Hz nodal geophones on the surface above and around a longwall coal mine from 30 June to 2 August 2018 (dataset B of Johnson *et al.*, 2021). Of the 17 stations, 14 were deployed close by forming a 1 km by 0.5 km semigrid on top of the active mining area (Fig. 1). The longwall orientation is nearly to east–west, and the approximate length of the mining wall is 250 m. The coal extraction activity moves along from north to south, and during our deployment, it advanced around 200 m south. The mine operator provided the longwall locations as measured by the surveyors every few days. A catalog of approximately 22,000 seismic events is also available (Johnson *et al.*, 2021), with local magnitudes ranging from −1.7 to 1.4.

The spectrogram of the vertical component at station 7 (Fig. 3) reveals the active nature of the mining environment. While we see stable and continuous background noise at the secondary microseism band (~5–10 s; Stehly *et al.*, 2006), we observe sporadic mining-related seismic energy in frequencies higher than 1 Hz. Although these energetic signals likely are associated with the mining induced seismic events, they can also be related to the shearing machinery, ore crushers, or heavy trucks. In the first seven days of July, this high-frequency energy is not as apparent or nearly absent. The activities pick up considerably after 7 July after the long weekend holiday of the United States Independence Day.

METHODS

Cross correlations

To investigate temporal CCF variation, we follow the methodology described by Wu *et al.* (2019, 2021) to first calculate the vertical component 5-min CCFs between all station pairs. Here, we cut the continuous data into 5-min nonoverlapping windows and perform spectral normalization before calculating the CCFs. We then stack the 5-min 1–5 Hz band-passed CCFs into the desired length in time (i.e., hourly stack and daily stack). We focus on the 1–5 Hz frequency band in this study, which presents the most coherent and persistent signals. To retain the relative CCF amplitude across the entire array (Lin *et al.*, 2012; Bowden *et al.*, 2015), each 5-min CCF was normalized based on the 90th percentile maximum amplitude of the CCFs across the entire array for that 5-min window before stacking. We note that although the normalization process is applied to down-weight sporadic but energetic events, persistent events that excited coherent cross-correlation signals can still dominate the stacked CCF.

Figure 4 shows the 5-min CCF variations for station pairs 6–3 and 7–14 on 26 July. Clear and coherent arrivals above the noise level throughout the day can be observed. Most energetic signals arrive close to zero lag time, reflecting the nature of the close station spacing and the fact that some noises originated from mining activities within the array. Close inspection reveals apparent temporal CCF variations particularly when comparing the CCF waveforms from earlier and later during the day (Fig. 4). The 5-min CCFs exhibit a lower signal-to-noise ratio (SNR) during the second half of the day, consistent with the weaker and presumably less coherent 1–5 Hz energy observed in the spectrogram (Fig. 3).

Separating the mining-related energy and the background noise

In addition to SNR, we observed that the CCF waveforms are different between the quiescent and operating time periods (e.g., white traces in Fig. 4a,b). The remarkable difference can be identified based on visual observation and from a single station pair. We also observe that the daily stack (Fig. 4c,d) of all the 5-min windows shows features more related to the mining time than the quiet time suggesting cross-correlation signals excited by mining activities are rather coherent. This

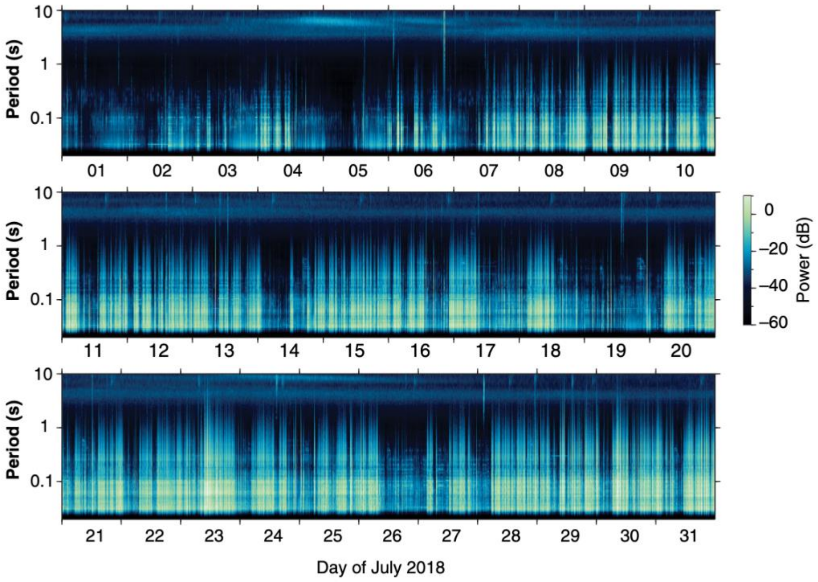

Figure 3. Month-long spectrogram of the vertical component recorded by station 7 (shown in Fig. 1). Power in decibel (dB) units of 10log (10) $(\mathrm{m}^2/\mathrm{s}^4/\mathrm{Hz})$. The color version of this figure is available only in the electronic edition.

motivates us to isolate the mine activity from the background noise based on the waveform similarity.

We use the correlation coefficient between the monthly stacked CCF and each 5-min CCF of a reference station pair 7–14 to separate the time windows dominated by mine energy (Fig. 5). We choose station pair 7–14 for two reasons. First, station 7 is the closest station to the mining operation and station 14 is outside the active mining area but on the coal extraction axis. Using this station pair, we ensure the 5-min CCFs capture the mining-related energy if present and that the waveform will be consistent during the deployment (Fig. 6b). Second, the interstation distance between the two stations (~0.9 km) is large such that there is more complexity in the reference stacked waveform due to slightly offset seismic phases. Assuming seismic signals excited by mining activity are self-similar and dominate the reference stacked CCF, 5-min time windows influenced by mine activity should yield CCFs with higher correlation coefficient. On the other hand, lower correlation coefficients are expected for time windows associated with weaker and less coherent background noise.

Figure 5a summarizes the evolution of the correlation coefficient between 5-min CCFs and the reference CCF for station pair 7–14 over the entire month of July. Low and high correlation coefficients are observed in early and late July, respectively, consistent with the progressive mine extraction operation and recorded seismicity (Fig. 3). A dip in correlation coefficient is observed around 19 July coinciding with the lower seismicity observed around the same time (Fig. 3). This demonstrates the CCF correlation coefficient as an effective indicator for mining induced signals. A simple statistical analysis of the plotted histograms reveals a bimodal distribution of the correlation coefficients from all the 5-min time windows (Fig. 5b). Here we select correlation coefficient of 0.4 to empirically separate all the time windows into two groups.

For each station pair, we stack the CCFs into daily CCFs using the high (>0.4) and low (<0.4) correlation coefficient time windows determined based on the reference station pair 7–14. For station pair 7–14, the daily stack of low correlation coefficient time windows (Fig. 5a) overall shows signals with low SNR. In contrast, the high correlation coefficient daily stack (Fig. 6b) shows a prominent and steady arrival close to 1 s. The result of station pair 6–3 is shown in Figure 6c,d, where the low correlation coefficient stack shows a stationary waveform between 0 and 1 s lag time throughout the entire period (Fig. 6c). This group of stacked waveforms is consistent with a steady background noise energy during the deployment. In contrast, the high correlation coefficient stack shows a progressive change in the waveform, with the dominant CCF signal shifting from negative time lag at the beginning of July to positive time lag at the end of the same month (Fig. 6d). Here a positive time lag represents seismic sources are closer to the CCF source station (station 6), whereas a negative time lag represents sources are closer to the receiver station (station 3). The change in arrival time for this group of waveforms is in agreement with the progressive movement of the longwall from the north (closer to receiver station 3) to the south (closer to source station 6). The observed stationary and progressively changing waveforms (Fig. 6) suggest that our classification based on correlation coefficient is successful in isolating time windows dominated by mining related signals and background noise.

Locating the mining activity

To further investigate the nature of temporal variations of CCF signal associated with the mining activities, we applied a CCF back projection method to determine the source location (Shapiro *et al.*, 2006; Zheng *et al.*, 2011; Ballmer *et al.*, 2013; Li *et al.*, 2020). For a given reference velocity, the method back

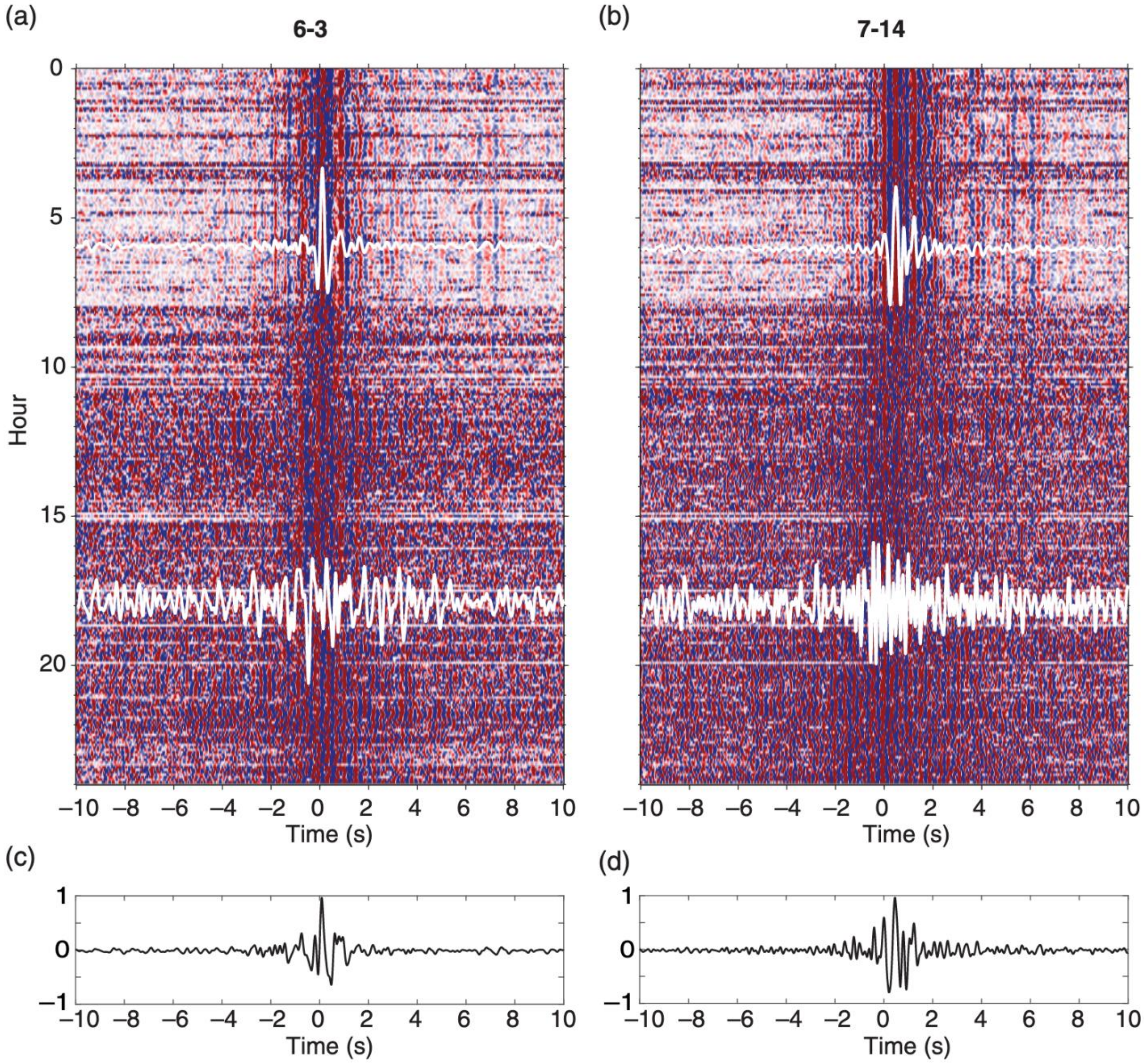

Figure 4. (a) Temporal variation of 5-min cross-correlations functions (CCFs) of station pair 6–3 on 7/26. Positive and negative CCF amplitudes are shaded in different tones to highlight the coherency through time. The white waveforms are the 5-min CCFs at 6:00 and 18:00. (b) Same as panel (a) but for station pair 7–14, (c) 7/26 daily CCF stack of station pair 6–3, and (d) 7/26 daily CCF stack of station pair 7–14. The color version of this figure is available only in the electronic edition.

projects seismic energy observed in the CCFs of all station pairs and determines the most likely area of the sources. The method has the advantage of mapping concurrent seismic sources simultaneously and the determined likelihood function would intrinsically account for the imperfect knowledge of the local velocity model and the source mechanism or area (Kao and Shan, 2004). For a single station pair, the migrated amplitudes form a hyperbola-shaped area that illuminates the potential source locations (Zheng *et al.*, 2011).

To determine the appropriate reference velocity for the area, for each 100 m distance bin, we stack all CCFs from a quiet day (7/5) across the entire array with station pair distance within the bin. This stacking process effectively homogenizes the noise source distribution and allows a clear CCF moveout to be observed (Fig. 7). Based on the observed moveout, we take 1 km/s as the reference velocity for our back projection analysis. Considering that the objective of this work is to obtain the overall temporal and spatial patterns of the seismic energy generated by the mining processes, we do not intend to resolve earth structure based on the observed moveout nor identify the wave type.

To perform 2D back projection, we build a potential source grid centered on station 7 with 0.001° (~100 m)

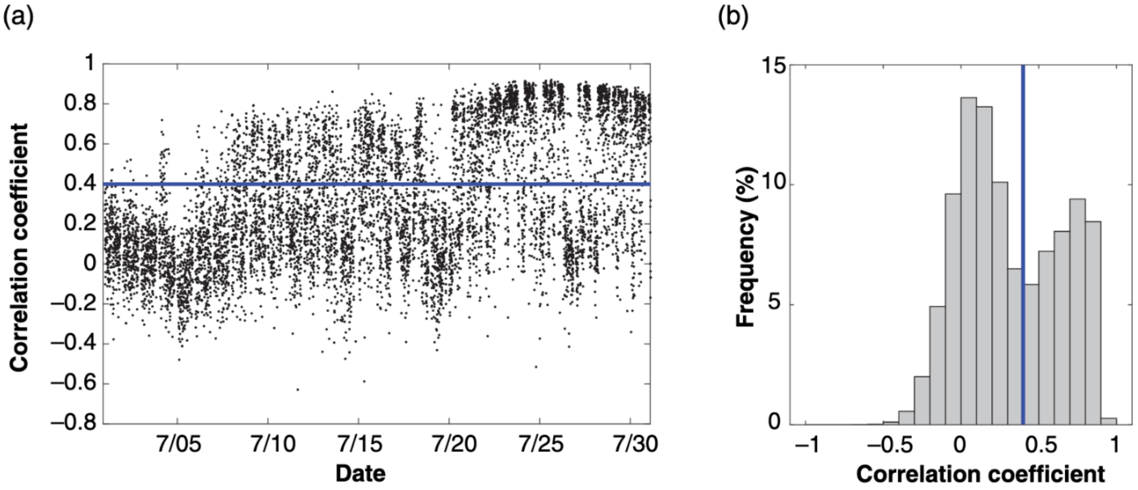

Figure 5. (a) Correlation coefficient between the 5-min CCFs and the monthly stacked CCF for station pair 7–14. The solid line denotes the 0.4 correlation coefficient which roughly separates time windows dominated by mine activity and background noise. (b) Histogram of correlation coefficient from panel (a). The solid line denotes the 0.4 correlation coefficient. The color version of this figure is available only in the electronic edition.

spacing in the north–south and east–west direction. For each potential source grid point, we calculate the expected arrival time for each station based on the straight ray distance. The differential time between any two stations is then used to estimate the expected lag time of the CCF signal for the station pair. For a given station pair, for each grid point, the corresponding amplitude at the expected lag time of the observed CCF normalized envelope function is assigned to the grid point as the likelihood value. By iterating these steps across the entire grid, the process effectively migrates or backprojects the envelope function to a 2D likelihood map (Fig. 8).

The use of the envelope function (instead of the raw CCF waveform) allows us to focus on the migration of seismic energy, which in general produces a more stable and smooth result considering the uncertainties associated with the reference velocity model and source mechanism (Dales *et al.*, 2017a). To further constrain the source locations, we sum all the resulting migrated 2D likelihood maps using all the station pairs with CCF SNR above 2. Here the signal and noise level are defined by the root mean square CCF amplitude within and outside the signal window, respectively. The signal window is determined by the expected minimum and maximum lag time calculated based on the distance and the reference velocity (Fig. 8). After the summation, we normalize the likelihood 2D map based on the maximum value, where areas with higher amplitude indicate the likely source locations (Figs. 9 and 10). Some smoothing is expected due to the finite width of the envelope function and some smearing is also expected for locations close to the edges of the array due to imperfect station coverage.

RESULTS AND DISCUSSION

Location from daily and 5-min cross correlations

The 2D back projection images based on the 1–5 Hz daily-stack CCFs reveal a spatial pattern that strongly agrees with the cataloged daily seismicity, a good proxy for the mining activity, with most of the seismicity contained within the 0.8 contour of the normalized back projection amplitude (Fig. 9 and Movie S1, available in the supplemental material to this article; Johnson *et al.*, 2021). The locations of both the seismicity and the resolved source distribution shift from north to south throughout the deployment period, consistent with the progression of the longwall (Fig. 1).

Compared to the daily stacked waveforms, back projection using 5-min time windows presents the opportunity to track seismicity migration with higher spatiotemporal resolution despite the lower SNR. In Figure 10, results from four example 5-min time windows on 7/26 are presented. Like the daily result, a good correlation between the back projection and the cataloged seismicity is observed. For the case where the seismicity is abundant and clustered (Fig. 10a,b), the area with normalized amplitude larger than 0.9 covers nearly all the event locations. For the rest of the events, the locations are within 0.7 and 0.8 normalized amplitude. For the case with sparser and distributed seismicity (Fig. 10c,d), all the seismicity is located within the area of greater than 0.8 normalized amplitude.

The good agreement between the cataloged seismicity and both the 5-min and daily backprojection results suggests that the interferometry based back projection method performs well, can robustly retrieve the location of the dominant seismic energy, and has the flexibility to tune the time resolution to fulfill different monitoring purposes. Our result in particular implies the framework is suitable for tracking the seismic source

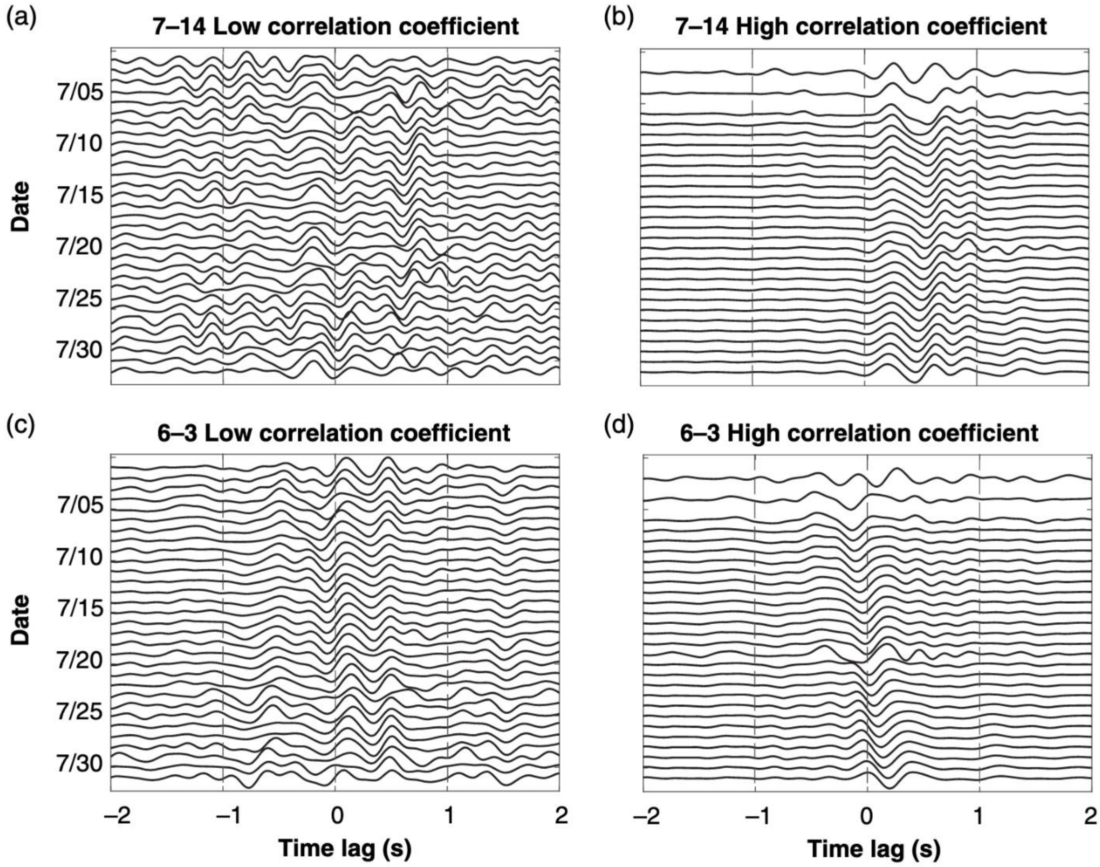

Figure 6. Daily stack for station pair (a,b) 7–14 and (c,d) 6–3. (a,c) Cross correlation with correlation coefficient lower than 0.4. (b,d) Cross correlation with correlation coefficient higher than 0.4.

evolution within an active mining environment. Different from the event catalog, which relies on the ability to pick seismic phases for individual events, the interferometry based back projection method presented in this study determines the overall source location during each specific time window. Although the spatiotemporal resolution might not be as high as the event catalog, the interferometry method has the ability to pick up weak but persistent energy and can easily be automated. Rather than a substitute, this method could be used as a complementary tool to better track nonimpulsive energies during mining operation (e.g., longwall operation).

Depth location

In the section Location From Daily and 5-min Cross Correlations, we demonstrate the overall agreement between the cataloged seismicity and our 2D back projection result on both 5-min and daily time scales. Here we explore further whether the method is capable of resolving the source location in 3D. Instead of assuming a 2D wave propagation, we consider body waves as the dominant seismic energy observed in the CCFs where straight ray paths again are assumed. We note that as most seismic sources are rather shallow and are directly beneath the seismic array, different wave types (*P* wave, *S* wave, and surface waves) are likely entangled and indistinguishable in the CCFs.

To extend our method to 3D, we add the vertical dimension to the original 2D potential source grid. For each 3D grid point and station, we calculate the source receiver travel time based on the 3D distance and the 1 km/s reference velocity. Here we take the station elevation into account. This change in computation will transform the shape of an individual CCF migration from a 2D hyperbola into a 3D hyperboloid (Fig. 11). Then we apply the same summation process described in the Locating the mining activity section. Here the amplitude normalization is based on the maximum value of the migrated 3D grid.

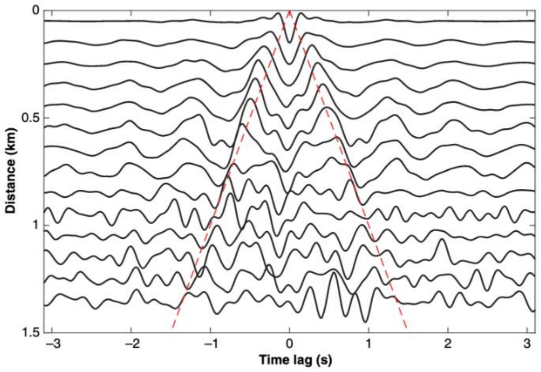

Figure 7. Bin stacked CCF record section. All available CCFs on 5 July are used. The dashed lines depict the 1 km/s reference velocity used in the back projection analysis. The color version of this figure is available only in the electronic edition.

We take the same 5-min time window as in Figure 9b (00:15–00:20 of 7/26) to demonstrate the 3D back projection result (Fig. 12). Like the 2D case, a good agreement is observed between the likelihood area and the cataloged event locations. The majority of the cataloged seismicity is contained by the 0.9 normalized amplitude area. Comparing the locations at 0, 200, and 400 m depth (Figs. 10b and 12a,b), the 3D back-projection shows an advantage in ruling out the deeper sources (>500 m); however, sources at shallow depth cannot be distinguished as the high likelihood area in general is elongated vertically and dips slightly toward the northwestern direction. The overall lower vertical resolution near the surface compared to the lateral resolution is expected for shallow sources considering the shape of 3D hyperboloids with both foci at the surface (Fig. 11).

The 3D result provides some constraints to the source depth, despite the maximum likelihood area being slightly shallower than the cataloged event depths. The maximum amplitude in

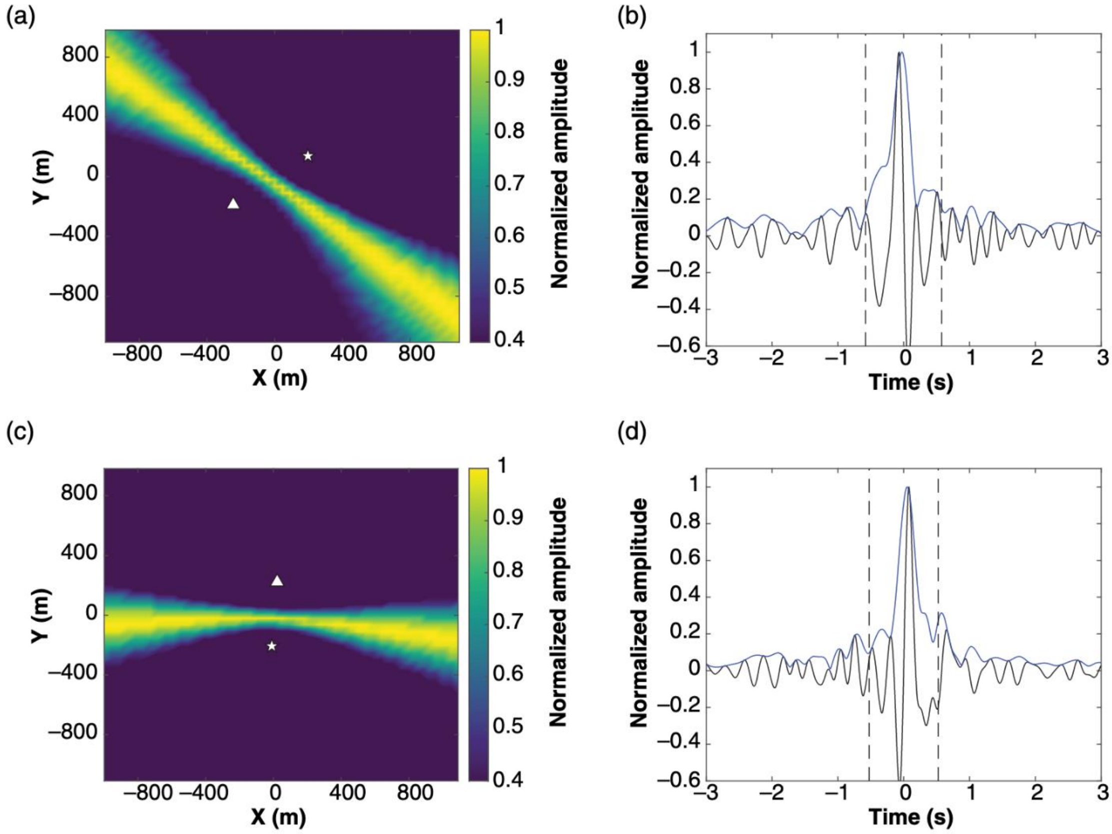

Figure 8. (a) The likelihood source location map derived from the 2D back projection of an example 5-min CCF of station pair 8–5. The star and the triangle depict the virtual source (station 8) and the receiver (station 5), respectively. (b) The 5-min CCF waveform (black line) and envelope (blue solid line) used in panel (a). The dashed lines denote the signal time window used in the back projection, which is determined based on the source–receiver distance and the 1 km/s reference velocity. (c,d) Same as panels (a,b) but for station pair 6–3. The color version of this figure is available only in the electronic edition.

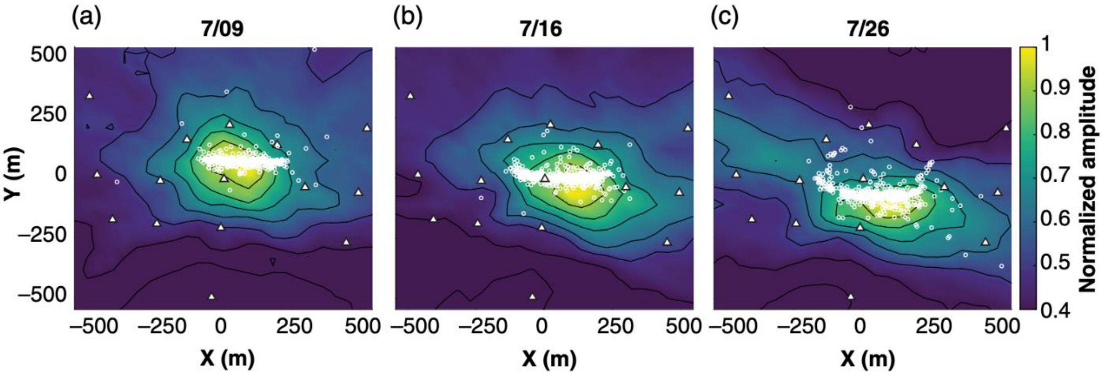

Figure 9. The likelihood source location maps on (a) 7/09, (b) 7/16, and (c) 7/26 derived from 2D back projection using all daily CCFs. The white open circles depict the corresponding daily seismicity, white triangles represent the stations, and the contours are plotted with an increment of 0.1 normalized amplitude. The rest of the days are shown in Movie S1. The color version of this figure is available only in the electronic edition.

Figure 12b,d is around 150–200 m, whereas the cataloged seismic activity is between 200 and 250 m depth. In addition to intrinsic low vertical resolution, the use of a homogeneous reference velocity and the likely entanglement of different wave types can also contribute to the apparent discrepancy. We note that our result nevertheless rules out deep sources consistent with mostly shallow mining related activities. The depth resolution (e.g., the plausible area with normalized amplitude >0.9) of the 3D result is larger than the 2D lateral resolution by a factor of 3, and the 3D computation time increases dramatically compared to 2D due to the 3D grid search. Consequently we feel the 2D framework might be more robust and better suited for automated seismic monitoring in a variety of environments (e.g., volcanic, geothermal, hydrothermal, mining, and wastewater or CO^2 injection) although 3D analysis can be used to provide additional depth constraints.

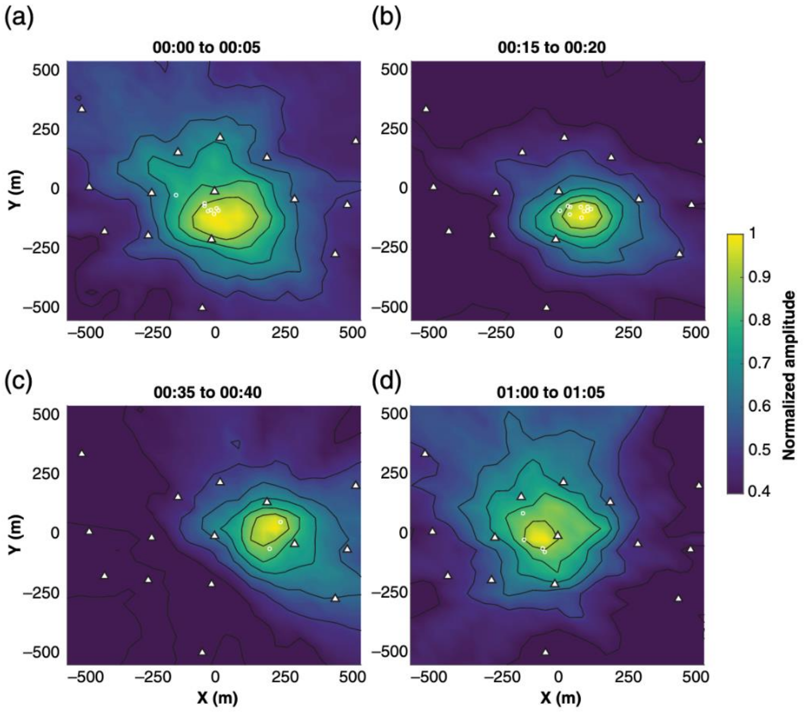

Figure 10. Same as Figure 9 but for 5-min CCFs on 26 July. (a) From 00:00 to 00:05. (b) From 00:15 to 00:20. (c) From 00:35 to 00:40. (d) From 01:00 to 01:05. The color version of this figure is available only in the electronic edition.

CONCLUSIONS

We collected one month of passive seismic data from a surface array above an active longwall coal mine. The continuous seismic recording dominantly consists of long-period (5–10 s) energy from microseism and short-period

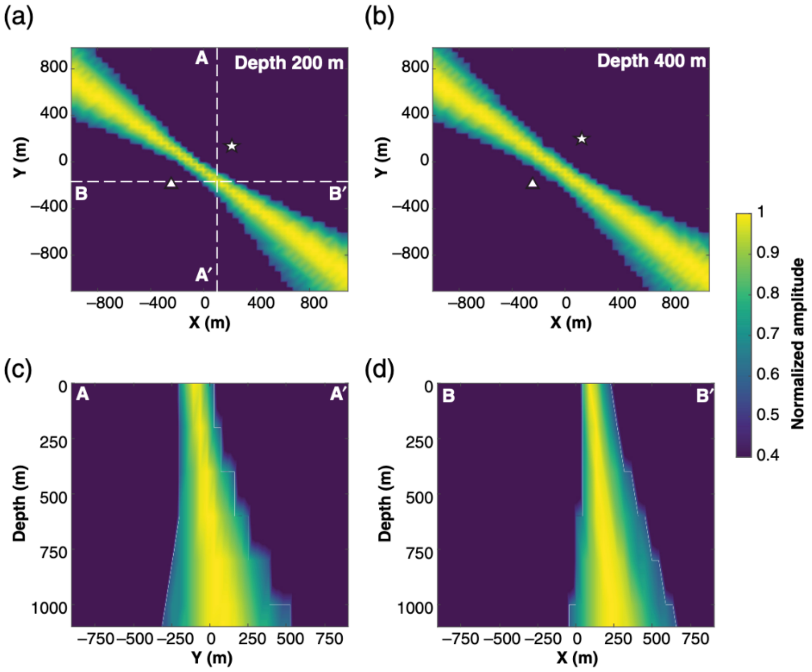

Figure 11. Similar to Figure 8a but for 3D back projection. (a,b) The likelihood normalized amplitude maps at 200 and 400 m depths. (c,d) The north–south cross section (A–A′ profile in panel a) and the east–west cross section (B–B′ profile in panel a), respectively. The color version of this figure is available only in the electronic edition.

(>1 Hz) energies from induced seismicity, industrial equipment, and background noise. We present a method to separate the mining-related activity from background noise by seismic interferometry and waveform similarity. Specifically, we classify the correlation coefficients between the monthly stacked CCFs and the consecutive 5-min window CCFs into two groups. The low correlation coefficient CCFs correspond to time windows dominated by background noise and are mostly stationary over time. In contrast, the high correlation coefficient CCFs correspond to time windows with mine activity and exhibit a temporal variation in line with the progression of the mining operation.

We migrate and back project the 5-min and daily cross-correlation wave packets from the high correlation coefficient time windows to locate the underground mining activity throughout the one-month deployment period. The resolved locations from both time resolutions correlate well with the cataloged seismic activity of the mine and the evolution of the longwall location. We show that our analysis has the ability to distinguish source clusters that are 200 m and 5 min apart. The consistency between the resolved noise location, seismicity, and longwall progression indicates the ability of the method to track small changes in source migration. The interferometry and back projection approach presented in this study can be a low-cost, computationally inexpensive, and reliable framework to monitor and distinguish seismic sources in an active environment (e.g., mine, volcano, geothermal or hydrothermal system, fracking or wastewater injection site, and oil or gas extraction area). Further work is needed to characterize and locate seismic activity of higher frequency where scattering and multipathing effects need to be accounted for. The background noise CCFs isolated from time windows with mining activity can be used to study temporal structural variation that might be sensitive to the mine caving process.

DATA AND RESOURCES

Raw data were collected at the mine site under conditions of anonymity and therefore cannot be released to the public. Cross-correlation functions (CCFs) are available upon request and decontextualized event waveforms are available at https://doi.org/10.7910/DVN/5DGFJB. Most of the plots were made using MATLAB v. 9.7.0.1190202 (R2019b). The supplemental material contains a video showing the likelihood source location maps from 2D back projection using daily stacks of CCFs (complement to Fig. 8). The white open circles depict the corresponding daily seismicity, the white triangles represent the stations, and the contours are plotted with an increment of 0.1 normalized amplitude.

DECLARATION OF COMPETING INTERESTS

The authors acknowledge that there are no conflicts of interest recorded.

ACKNOWLEDGMENTS

The authors thank the Associate Editor and two anonymous reviewers for their constructive comments to improve the article. The authors gratefully acknowledge the National Institute for Occupational Safety and Health (NIOSH) and an anonymous collaborating mine site for permitting us to use this dataset. This study was supported by the National Science Foundation (NSF) Grant EAR 1753362 and NIOSH project 19IPA1916693. S. R. acknowledges a scholarship by the *Consejo Nacional de Ciencia y Tecnología* (CONACYT; Scholarship Number 710069). The findings and conclusions in this

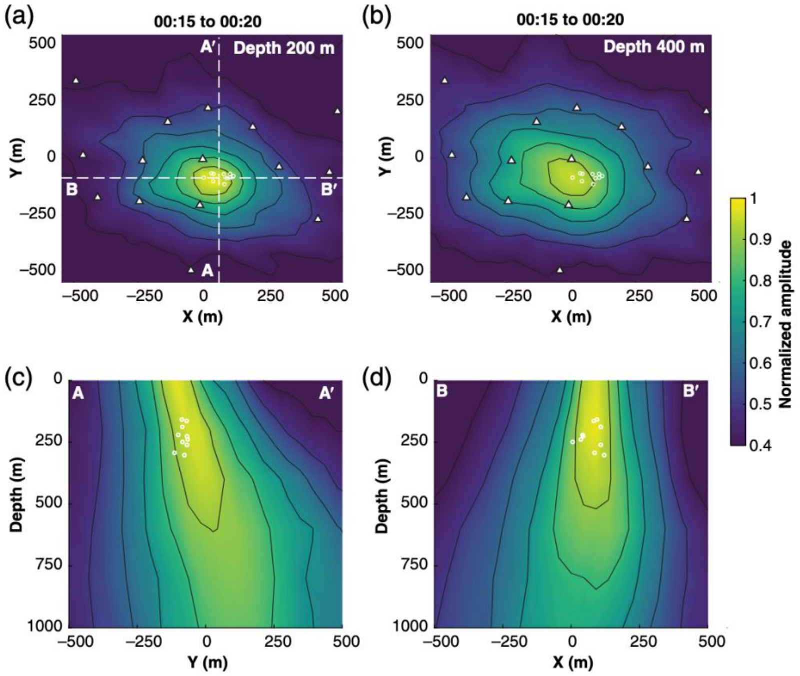

Figure 12. Similar to Figure 10b but for 3D back projection. (a,b) The likelihood normalized amplitude maps at 200 and 400 m depths. (c,d) The north–south cross section (A–A′ profile in panel a) and the east–west cross section (B–B′ profile in panel a), respectively. The color version of this figure is available only in the electronic edition.

report are those of the author(s) and do not necessarily represent the official position of the National Institute for Occupational Safety and Health, Centers for Disease Control and Prevention. Mention of any company or product does not constitute endorsement by NIOSH, CDC.

REFERENCES

Ballmer, S., C. J. Wolfe, P. G. Okubo, M. M. Haney, and C. H. Thurber (2013). Ambient seismic noise interferometry in Hawai'i reveals long-range observability of volcanic tremor, *Geophys. J. Int.* **194,** no. 1, 512–523, doi: 10.1093/gji/ggt112.

Bischoff, M., A. Cete, R. Fritschen, and T. Meier (2010). Coal mining induced seismicity in the Ruhr area, Germany, *Pure Appl. Geophys.* **167,** nos. 1/2, 63–75, doi: 10.1007/s00024-009-0001-8.

Brenguier, F., M. Campillo, C. Hadziioannou, N. M. Shapiro, R. M. Nadeau, and E. Larose (2008). Postseismic relaxation along the San Andreas fault at Parkfield from continuous seismological observations, *Science* **321,** no. 5895, 1478–1481, doi: 10.1126/science.1160943.

Bowden, D.C., V.C. Tsai, and F.-C. Lin, (2015). Site amplification, attenuation and scattering from noise correlation amplitudes across a dense array in Long Beach, *Geophys. Res. Lett.* **42,** 1360–1367, doi: 10.1002/2014GL062662.

Chen, B. R., X. T. Feng, X. Zeng, Y. Xiao, Z. Zhang, H. Ming, and G. Feng (2011). Real-time microseismic monitoring and its characteristic analysis during TBM tunneling in deep-buried tunnel, *Chin. J. Rock Mech. Eng.* **30,** no. 2, 275–283.

Clements, T., and M. A. Denolle (2018). Tracking groundwater levels using the ambient seismic field, *Geophys. Res. Lett.* **45,** no. 13, 6459–6465, doi: 10.1029/2018GL077706.

Cros, E., P. Roux, J. Vandemeulebrouck, and S. Kedar (2011). Locating hydrothermal acoustic sources at old faithful geyser using matched field processing, *Geophys. J. Int.* **187,** no. 1, 385–393, doi: 10.1111/j.1365-246X.2011.05147.x.

Czarny, R., H. Marcak, N. Nakata, Z. Pilecki, and Z. Isakow (2016). Monitoring velocity changes caused by underground coal mining using seismic noise, *Pure and Appl. Geophys.* **173,** no. 6, 1907–1916.

Dales, P., P. Audet, and G. Olivier (2017a). Seismic interferometry using persistent noise sources for temporal subsurface monitoring, *Geophys. Res. Lett.* **44,** no. 21, 10,863–10,870, doi: 10.1002/2017GL075342.

Dales, P., P. Audet, G. Olivier, and J. P. Mercier (2017b). Interferometric methods for spatio temporal seismic monitoring in underground mines, *Geophys. J. Int.* **210,** no. 2, 731–742, doi: 10.1093/gji/ggx189.

Eaton, D. W. (2018). *Passive Seismic Monitoring of Induced Seismicity: Fundamental Principles and Application to Energy Technologies*, Cambridge University Press, Cambridge, United Kingdom.

Haney, M. M. (2010). Location and mechanism of very long period tremor during the 2008 eruption of Okmok volcano from interstation arrival times, *J. Geophys. Res.* **115,** no. 10, 1–13, doi: 10.1029/2010JB007440.

Haney, M. M. (2014). Backprojection of volcanic tremor, *Geophys. Res. Lett.* **41,** no. 6, 1923–1928, doi: 10.1002/2013GL058836.

Johnson, S. W., D. J. Chambers, M. S. Boltz, and K. D. Koper (2021). Application of a convolutional neural network for seismic phase picking of mining-induced seismicity. *Geophys. J. Int.* **224,** no. 1, 230–240.

Kao, H., and S. J. Shan (2004). The source-scanning algorithm: Mapping the distribution of seismic sources in time and space, *Geophys. J. Int.* **157,** no. 2, 589–594, doi: 10.1111/j.1365-246X.2004.02276.x.

Li, K. L., H. Sadeghisorkhani, G. Sgattoni, O. Gudmundsson, and R. Roberts (2017). Locating tremor using stacked products of correlations, *Geophys. Res. Lett.* **44,** no. 7, 3156–3164, doi: 10.1002/2016GL072272.

Li, L., J. Tan, B. Schwarz, F. Staněk, N. Poiata, P. Shi, L. Diekmann, L. Eisner, and D. Gajewski (2020). Recent advances and challenges of waveform-based seismic location methods at multiple scales, *Rev. Geophys.* **58,** no. 1, 1–47, doi: 10.1029/2019RG000667.

Lin, F. C., M. P. Moschetti, and M. H. Ritzwoller (2008). Surface wave tomography of the western United States from ambient seismic noise: Rayleigh and Love wave phase velocity maps, *Geophys. J. Int.* **173,** no. 1, 281–298, doi: 10.1111/j.1365-246X.2008.03720.x.

Lin, F.-C., V. Tsai, and M.H. Ritzwoller (2012). The local amplification of surface waves: A new observable to constrain elastic velocities, density, and anelastic attenuation, *J. Geophys. Res.* **117,** no. B6, doi: 10.1029/2012JB009208.

Lobkis, O. I., and R. L. Weaver (2001). On the emergence of the Green's function in the correlations of a diffuse field, *J. Acoust. Soc. Am.* **110,** no. 6, 3011–3017, doi: 10.1121/1.1417528.

Lu, B., and J. Feng (2017). Coal working face imaging by seismic interferometry-using conveyer belt noise as source, *J. Seismol. Explor.* **26,** no. 5, 411–432.

Majer, E. L., R. Baria, M. Stark, S. Oates, J. Bommer, B. Smith, and H. Asanuma (2007). Induced seismicity associated with enhanced geothermal systems, *Geothermics* **36,** no. 3, 185–222, doi: 10.1016/j.geothermics.2007.03.003.

Maxwell, S. C., D. Raymer, M. Williams, and P. Primiero (2012). Tracking microseismic signals from the reservoir to surface, *The Leading Edge* **31,** no. 11, 1300–1308, doi: 10.1190/tle31111300.1.

Mendecki, A. J., R. A. Lynch, and D. A. Malovichko (2010). Routine micro-seismic monitoring in mines, *Australian Earthquake Engineering Society 2010 Conference*, November 2010, Perth, Australia, 1–33.

Nicolson, H., A. Curtis, and B. Baptie (2014). Rayleigh wave tomography of the British Isles from ambient seismic noise, *Geophys. J. Int.* **198,** no. 2, 637–655, doi: 10.1093/gji/ggu071.

Nordström, E., S. Dineva, and E. Nordlund (2020). Back analysis of short-term seismic hazard indicators of larger seismic events in deep underground mines (LKAB, Kiirunavaara mine, Sweden), *Pure Appl. Geophys.* **177,** no. 2, 763–785.

Sen, A. T., S. Cesca, M. Bischoff, T. Meier, and T. Dahm (2013). Automated full moment tensor inversion of coal mining-induced seismicity, *Geophys. J. Int.* **195,** no. 2, 1267–1281, doi: 10.1093/gji/ggt300.

Shapiro, N. M., M. Campillo, L. Stehly, and M. H. Ritzwoller (2005). High-resolution surface-wave tomography from ambient seismic noise, *Science* **307,** no. 5715, 1615–1618, doi: 10.1126/science.1108339.

Shapiro, N. M., M. H. Ritzwoller, and G. D. Bensen (2006). Source location of the 26 sec microseism from cross-correlations of ambient seismic noise, *Geophys. Res. Lett.* **33,** no. 18, 1–5, doi: 10.1029/2006GL027010.

Spica, Z., M. Perton, M. Calò, D. Legrand, F. Córdoba-Montiel, and A. Iglesias (2016). 3-D shear wave velocity model of Mexico and south US: Bridging seismic networks with ambient noise cross-correlations (C1) and correlation of coda of correlations (C3), *Geophys. J. Int.* **206,** no. 3, 1795–1813, doi: 10.1093/gji/ggw240.

Stec, K. (2007). Characteristics of seismic activity of the upper Silesian coal basin in Poland, *Geophys. J. Int.* **168,** no. 2, 757–768, doi: 10.1111/j.1365-246X.2006.03227.x.

Stehly, L., M. Campillo, and N. M. Shapiro (2006). A study of the seismic noise from its long-range correlation properties, *J. Geophys. Res.* **111,** no. 10, 1–12, doi: 10.1029/2005JB004237.

Swanson, P. L., M. S. Boltz, and D. Chambers (2016). Seismic monitoring strategies for deep longwall coal mines, Department of Health and Human Services Centers for Disease Control and Prevention National Institute for Occupational Safety and Health, Office of Mine Safety and Health Research Pittsburgh, Spokane, Washington.

Verdon, J. P., J. M. Kendall, A. Butcher, R. Luckett, and B. J. Baptie (2018). Seismicity induced by longwall coal mining at the Thoresby Colliery, Nottinghamshire, U.K., *Geophys. J. Int.* **212,** no. 2, 942–954, doi: 10.1093/gji/ggx465.

Verdon, J. P., J. M. Kendall, and S. C. Maxwell (2010). A comparison of passive seismic monitoring of fracture stimulation from water and CO2 injection, *Geophysics* **75,** no. 3, 1–7, doi: 10.1190/1.3377789.

Wu, S. M., F. C. Lin, J. Farrell, and A. Allam (2019). Imaging the deep subsurface plumbing of old faithful geyser from low-frequency hydrothermal tremor migration, *Geophys. Res. Lett.* **46,** no. 13, 7315–7322, doi: 10.1029/2018GL081771.

Wu, S. M., F. C. Lin, J. Farrell, W. E. Keller, E. B. White, and J. D. G. Hungerford (2021). Imaging the subsurface plumbing complex of steamboat geyser and cistern spring with hydrothermal tremor migration using seismic interferometry, *J. Geophys. Res.* **126,** no. 4, doi: 10.1029/2020JB021128.

Wu, S. M., F. C. Lin, J. Farrell, B. Shiro, L. Karlstrom, P. Okubo, and K. Koper (2020). Spatiotemporal seismic structure variations associated with the 2018 Kīlauea eruption based on temporary dense geophone arrays, *Geophys. Res. Lett.* **47,** no. 9, 1–10, doi: 10.1029/2019GL086668.

Wu, S. M., K. M. Ward, J. Farrell, F. C. Lin, M. Karplus, and R. B. Smith (2017). Anatomy of old faithful from subsurface seismic imaging of the Yellowstone upper Geyser basin, *Geophys. Res. Lett.* **44,**no. 20, 10,240–10,247, doi: 10.1002/2017GL075255.

Zheng, Y., W. Shen, L. Zhou, Y. Yang, Z. Xie, and M. H. Ritzwoller (2011). Crust and uppermost mantle beneath the north China craton, northeastern China, and the Sea of Japan from ambient noise tomography, *J. Geophys. Res.* **116,** no. 12, 1–25, doi: 10.1029/2011JB008637.

Manuscript received 3 March 2022

CHAPTER 3

THE CRUSTAL MAGMATIC STRUCTURE BENEATH THE DENALI VOLCANIC GAP IMAGED BY A DENSE LINEAR SEISMIC ARRAY

Rabade, S., Lin, F. C., Tape, C., Ward, K. M., Waldien, T., & Allam, A. (2023). The crustal magmatic structure beneath the Denali Volcanic Gap imaged by a dense linear seismic array. *Journal of Geophysical Research: Solid Earth*, 128(12), e2023JB027152.

JGR Solid Earth

RESEARCH ARTICLE
10.1029/2023JB027152

The Crustal Magmatic Structure Beneath the Denali Volcanic Gap Imaged by a Dense Linear Seismic Array

Santiago Rabade[1], **Fan-Chi Lin**[1], **Carl Tape**[2], **Kevin M. Ward**[3], **Trevor Waldien**[3], **and Amir Allam**[1]

[1]Department of Geology and Geophysics, University of Utah, Salt Lake City, UT, USA, [2]Geophysical Institute and Department of Geosciences, University of Alaska, Fairbanks, AK, USA, [3]Department of Geology and Geological Engineering, South Dakota School of Mines & Technology, Rapid City, SD, USA

Key Points:

- We present a 2-D shear velocity model of the top 16 km of the crust in south-central Alaska across the Alaska range
- The Denali fault was identified as a narrow localized low-velocity anomaly extending to at least 12 km depth
- We observe a low-velocity zone ~12 km beneath the volcanic gap. We interpret the anomaly as a subduction-related magma reservoir

Correspondence to:

S. Rabade,
san.rabade@utah.edu

Citation:

Rabade, S., Lin, F.-C., Tape, C., Ward, K. M., Waldien, T., & Allam, A. (2023). The crustal magmatic structure beneath the Denali Volcanic Gap imaged by a dense linear seismic array. *Journal of Geophysical Research: Solid Earth*, *128*, e2023JB027152. https://doi.org/10.1029/2023JB027152

Received 23 MAY 2023
Accepted 22 NOV 2023

Author Contributions:

Conceptualization: Fan-Chi Lin, Carl Tape, Kevin M. Ward, Amir Allam
Formal analysis: Santiago Rabade, Trevor Waldien, Amir Allam
Funding acquisition: Carl Tape, Kevin M. Ward, Amir Allam
Investigation: Santiago Rabade
Methodology: Santiago Rabade, Fan-Chi Lin, Amir Allam
Project Administration: Fan-Chi Lin, Carl Tape, Kevin M. Ward, Amir Allam
Resources: Carl Tape
Software: Santiago Rabade, Fan-Chi Lin
Supervision: Fan-Chi Lin, Carl Tape, Kevin M. Ward
Validation: Santiago Rabade
Visualization: Santiago Rabade
Writing – original draft: Santiago Rabade, Fan-Chi Lin
Writing – review & editing: Carl Tape, Kevin M. Ward, Trevor Waldien

Abstract

The crustal structure in south-central Alaska has been influenced by terrane accretion, flat slab subduction, and a modern strike-slip fault system. Within the active subduction system, the presence of the Denali Volcanic Gap (DVG), a ~400 km region separating the active volcanism of the Aleutian Arc to the west and the Wrangell volcanoes to the east, remains enigmatic. To better understand the regional tectonics and the nature of the volcanic gap, we deployed a month-long north-south linear geophone array of 306 stations with an interstation distance of 1 km across the Alaska Range. By calculating multi-component noise cross-correlation and jointly inverting Rayleigh wave phase velocity and ellipticity across the array, we construct a 2-D shear wave velocity model along the transect down to ~16 km depth. In the shallow crust, we observe low-velocity structures associated with sedimentary basins and image the Denali fault as a narrow localized low-velocity anomaly extending to at least 12 km depth. About 12 km, below the fold and thrust fault system in the northern flank of the Alaska Range, we observe a prominent low-velocity zone with more than 15% velocity reduction. Our velocity model is consistent with known geological features and reveals a previously unknown low-velocity zone that we interpret as a magmatic feature. Based on this feature's spatial relationship to the Buzzard Creek and Jumbo Dome volcanoes and the location above the subducting Pacific Plate, we interpret the low-velocity zone as a previously unknown subduction-related crustal magma reservoir located beneath the DVG.

Plain Language Summary

The Alaska Range in south-central Alaska has been shaped by different geological processes. One puzzling aspect is the Denali Volcanic Gap, a region of about 400 km between the Aleutian Arc and the Wrangell volcanoes. To understand this volcanic gap and regional tectonics better, we obtained a 2-D model of shear wave velocity down to a depth of about 16 km, using a month-long linear geophone array with over 300 stations placed at 1 km intervals across the Alaska Range. In the shallow crust, we found areas with low-velocity associated with sedimentary basins. We observe a narrow anomaly related to the Denali fault with low-velocity extending to at least 12 km depth. About 12 km below the northern flank of the Alaska Range, we discovered a significant zone with low seismic velocities. This zone is believed to be related to magma and is located above the subducting Pacific Plate. We interpreted the anomaly as a magma reservoir beneath the volcanic gap, based on its tectonic and spatial relationship with nearby volcanoes.

1. Introduction

The south-central region of Alaska has a complex and active tectonic setting (Figure 1a). The low-angle flat subduction of the Pacific plate and the buoyant Yakutat slab transmit oblique convergence inland, causing counterclockwise rotation of south-central Alaska and orogenesis of the Alaska Range (Bemis et al., 2012; Freymueller et al., 2008; Haeussler, 2008). Most of the rotation is accommodated by the Denali fault (DF), a dextral strike-slip fault that accommodates about 20% of the convergence between the Pacific Plate/Yakutat terrane and the North American Plate (Matmon et al., 2006; Pavlis et al., 2004). The DF developed within the Alaska Range suture zone (SZ), the product of the oblique collision of allochthonous oceanic terranes in the south to the pericratonic terranes in the north (Ridgway et al., 2002).

The heterogeneous composition of the SZ crust reflects the nature of its origin. The metamorphic and sedimentary rocks of the SZ in Central Alaska, known as the Kahiltna assemblage, can be divided into northern and southern succession, with affinity to the Yukon Composite Terrane (YCT) (continental crust) and Wrangelia composite terrane (oceanic crust), respectively (Clautice, Newberry, Blodgett, et al., 2001; Clautice, Newberry,

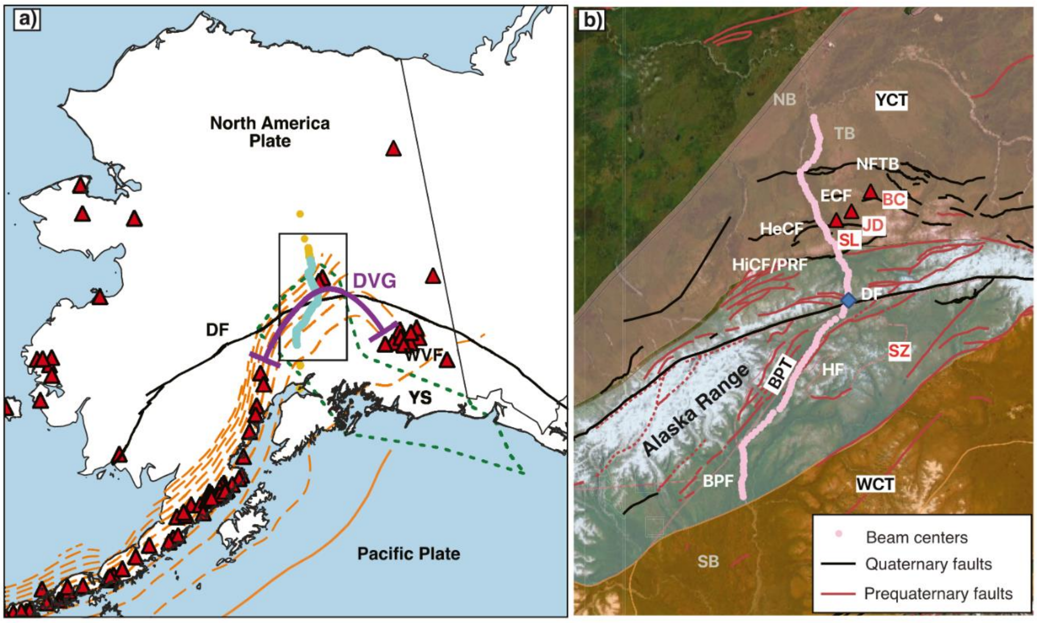

Figure 1. (a). Tectonic setting of Alaska. North America-Pacific convergent plate boundary (solid orange line) and slab depth contours (orange dashed lines) (Hayes et al., 2018). Other features include the geometry of the Yakutat Slab (YS) (green dashed outline) (Eberhart-Phillips et al., 2006), the Denali fault (DF) (black line), the Wrangell Volcanic Field (WVF), volcanoes (red triangles), nodal stations (cyan circles), broadband stations (yellow circles) used in this study. The purple line denotes the extension of the Denali Volcanic Gap (DVG). The black rectangle denotes the location of the right inset. (b). Location of the imaged region. Beam centers (light pink circles: 106 total), volcanoes (red triangles), Quaternary faults (black lines) (Koehler et al., 2013), and pre-Quaternary faults (red lines) (Koehler et al., 2012). The blue diamond identifies the beam used as an example in Figures 3–5, 7^{3-5}, and 8. The gray labels are the major basins mentioned in the text: Susitna basin (SB), Nenana basin (NB), and Tanana basin (TB). The white labels are faults mentioned in the text: Broad Pass fault (BPF), Hurricane fault (HF), Denali fault (DF), Hines Creek fault/Parks Road fault (HiCF/PRF), Healy Creek Fault (HeCF), Ealy Creek fault (ECF), Northern Foothills Thrust Belt (NFTB). The red labels are volcanic features mentioned in the text: Jumbo Dome (JB), Buzzard Creek (BC), and Sugar Loaf Mountain (SL). The black labels are the Broad Pass Terrane (BPT), Wrangellia Composite Terrane (WTC, orange), suture zone (SZ, light blue), and the Yukon Composite Terrane (YCT, pink).

Pinney, et al., 2001; Hampton et al., 2010) (Figure 1). Both Kahlitna successions have rocks from volcanism and intrusions from the subduction-related arc and collisional magmatism (Romero et al., 2020); some of these rocks form the Broad Pass Terrane (BPT) (Clautice, Newberry, Blodgett, et al., 2001; Clautice, Newberry, Pinney, et al., 2001). The terranes north of the SZ are commonly referred to as the YCT, consisting of metamorphosed rocks of the former continental margin (Ridgway et al., 2002). The Hines Creek fault (HiCF), which likely extends to the bottom of the crust, is the northern margin of the SZ (Brennan et al., 2011) separating the accreted terranes to the south and the former continental margin to the north (Ridgway et al., 2007). Recent studies of the HiCF have shown the lack of lateral offsets on the fault while noting some near-vertical offsets (Bemis et al., 2012, 2015), in contrast to more than 480 km of dextral displacement of the DF (Waldien et al., 2021). The trace of the DF follows the Alaska Range and SZ (Haeussler, Matmon, et al., 2017).

Despite the active subduction of the Pacific-Yakutat slab beneath the area (Martin-Short et al., 2018), low volcanic activity is present within the Denali Volcanic Gap (DVG), a ∼400 km region separating the active volcanism of the Aleutian Arc to the west and the Wrangell volcanoes to the east (Figure 1a). Whereas volcanic gaps are not unique to the Alaska subduction zone (e.g., Peru, Chile, Nankai, New Guinea) (Gutscher, Maury, et al., 2000), the DVG's origin remains enigmatic. Gutscher, Spakman, et al. (2000) argue that a low-angle flat subduction can interrupt mantle flow and inhibit arc volcanism. Chuang et al. (2017) propose that fluids are confined to only the uppermost part of the Yakutat crust, leading to an early release of fluids and a relatively anhydrous slab. Rondenay et al. (2010) propose the slab is generating melt but suggest the magmatic material does not rise to the surface but accumulates at the top of the mantle wedge. Alternatively, the melt might be accumulating in the crust, where the compressional stress or structures in the Alaska Range impede magma upwelling (McNamara & Pasayanos, 2002).

North of the DF, there are two isolated contemporary volcanic bodies and one fossilized volcanic vent. The Buzzard Creek (BC) maars consist of two craters, dated at ca. 10 ka with basalt composition similar to the volcanoes in the eastern Aleutian Arc and the Wrangell Volcanic Field (WVF) (Albanese, 1980; Andronikov & Mukasa, 2010; Nye et al., 2018; Wood & Kienle, 1990). The Jumbo Dome Volcano, south of the BC maars, is a hornblende andesite dome (Cameron et al., 2015) dated at ca. 1 Ma (Athey et al., 2006) and composition similar to the adakite geochemical signature common in Wrangell arc lavas (Brueseke et al., 2019). South of the Jumbo Dome is Sugar Loaf Mountain, a fossilized volcanic vent with rhyolite and andesite composition (Albanese, 1980; Cameron et al., 2015; Reger, 1980). It is worth noting that the depth of the subducted slab beneath these volcanic bodies is ∼100 km (Hayes et al., 2018), consistent with the global observations of slab-generating arc volcanism (Syracuse & Abers, 2006) independent of the thermal state of the slabs (Wada & Wang, 2009). The compositions of these bodies are similar to the volcanoes in the eastern Aleutian Arc and the western WVF, and the depth of the slab is ideal for arc volcanism, and therefore it is natural to consider an association with subduction (Albanese, 1980; Andronikov & Mukasa, 2010).

In this study, we use ambient seismic noise recorded by a 270 km long linear dense seismic array and image the 2D crustal structure down to 16 km depth across the Alaska Range. Leveraging the dense station coverage, our shear velocity image has a superior resolution compared with previous studies along the same profile in regional and continental studies using broadband stations (A. A. Allam et al., 2017; Berg et al., 2020; Eberhart-Phillips et al., 2006; Martin-Short et al., 2018; Rondenay et al., 2010; Y. Wang & Tape, 2014; Ward & Lin, 2018; X. Yang & Gao, 2020). The new model reveals detailed crustal features that were not imaged before, including a prominent middle crust low-velocity anomaly beneath the northern flank of the Alaska Range likely related to the magmatism associated with the DVG.

2. Data and Methodology

2.1. Data

In this study, we used ambient noise data from a semi-linear temporal nodal deployment and a handful of permanent stations installed along Parks Highway in South-Central Alaska (Figure 1). The temporal array consisted of 306 three-component 5 Hz geophones deployed from late February to early April in 2019 with a 1 km interstation distance (A. Allam et al., 2019). The southern end of the array is north of Anchorage near the town of Talkeetna, and the northern end is west of Fairbanks in the town of Nenana. To increase the number of measurements at the nodal stations, we use several existing broadband stations along the line as virtual sources and extend the array north and south, including seven stations from the FLATS array (2014–2019: Tape et al., 2018).

2.2. Ambient Noise Cross-Correlation

To calculate the three-component ambient noise cross-correlation, we follow Y. Wang, Allam, and Lin (2019). First, we remove the instrument response of all the stations, cut the data into 10-min segments, and whiten the three-component data simultaneously in the frequency domain based on the vertical spectrum. We then compute the nine-component cross-correlations between each station pair. Before stacking all the time windows, we normalize the multi-component cross-correlations by the maximum amplitude of the vertical-vertical component. For periods between 4 and 10 s, clear Rayleigh wave moveout can be observed in the cross-correlation record sections (e.g., Figure 2). The asymmetry of the cross-correlations indicates that the noise wavefield is dominantly propagating toward the north. Despite the inhomogeneous source distribution, the clear Rayleigh wave moveout suggests the noise wavefield is likely semi-diffusive and satisfies stationary phase approximation (Lin et al., 2008; Snieder, 2004; Y. Yang & Ritzwoller, 2008).

2.3. Rayleigh Phase Velocity and Ellipticity

We use beamforming (slant-stacking; Y. Wang, Allam, & Lin, 2019; Wells et al., 2022) to enhance the Rayleigh wave signals and to simultaneously determine location-dependent Rayleigh wave phase velocities (Figure 3) and

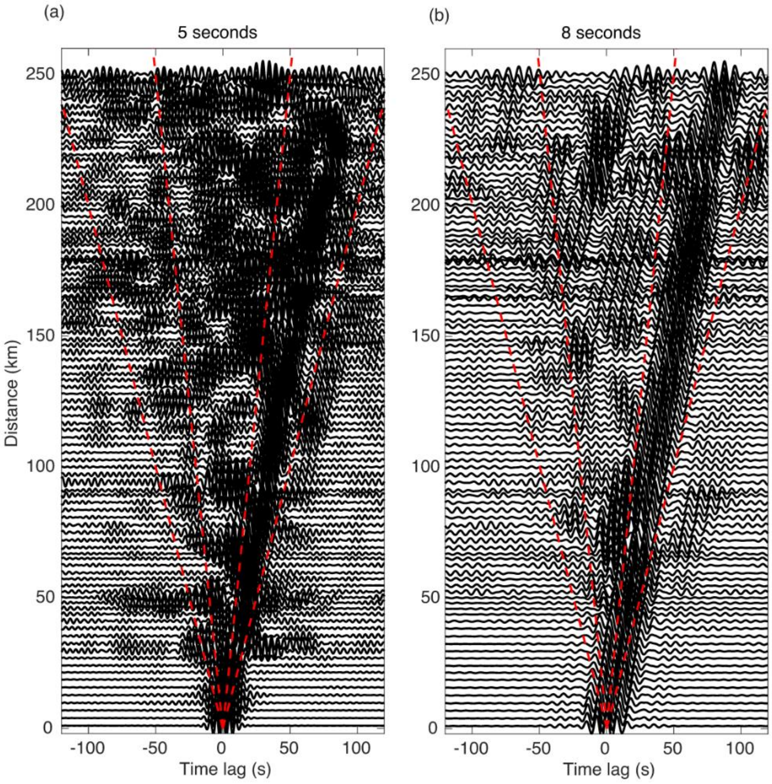

Figure 2. Example of noise cross-correlation record sections calculated for the vertical-vertical (ZZ) component between the southernmost nodal station (1001) and all the receiver stations filtered around (a) 5 s and (b) 8 s. Red dashed lines illustrate the reference velocity of 2 and 5 km/s. The higher amplitudes with positive time lags indicate that the noise is coming from the south of the array.

Rayleigh wave ellipticity or horizontal-to-vertical amplitude ratios (*H*/*V* ratio; Figure 4). The method determines surface wave properties at the receiver beam center, one source station at a time, by using cross-correlations between the source station and all receiver stations within the receiver beam. This is slightly different from the double beamforming technic (i.e., beams on both the source and receiver sides) presented by Y. Wang, Allam, and Lin (2019), Y. Wang, Lin, and Ward (2019), which works better when the array is closer to linear, and all ray paths are along the line. Compared to the traditional tomography method based on single station measurements, the beamforming approach has the advantage of improving signals that are close to or marginally above the noise level (e.g., Figure 2a). In this study, we include a total of 106 receiver beams in our analysis, that is one beam center per 0.02° latitude between 62.4°N and 64.5°N. The longitude of the beam center is determined by the averaged longitude of the two closest stations to that latitude. We use a 15 km beam diameter for the central part (between 63°N and 64.2°N), where coverage is best; in the northern and southern edges of the array (south of 63°N and north of 64.2°N), we use 30 km.

For each source-receiver pair, we first cut vertical-vertical (ZZ) and vertical-radial (ZR) cross-correlations based on a reference velocity of 7 km/s to remove early spurious arrivals (Y. Wang, Allam, & Lin, 2019; Y. Wang, Lin, & Ward, 2019; Yao et al., 2009). Next, we normalize the ZZ and ZR waveforms by the maximum ZZ amplitude. For each source station and all receiver stations within a receiver beam, we perform a grid search to find the best phase slowness that maximizes the envelope amplitude of the shifted and stacked ZZ waveforms (Figure 3).

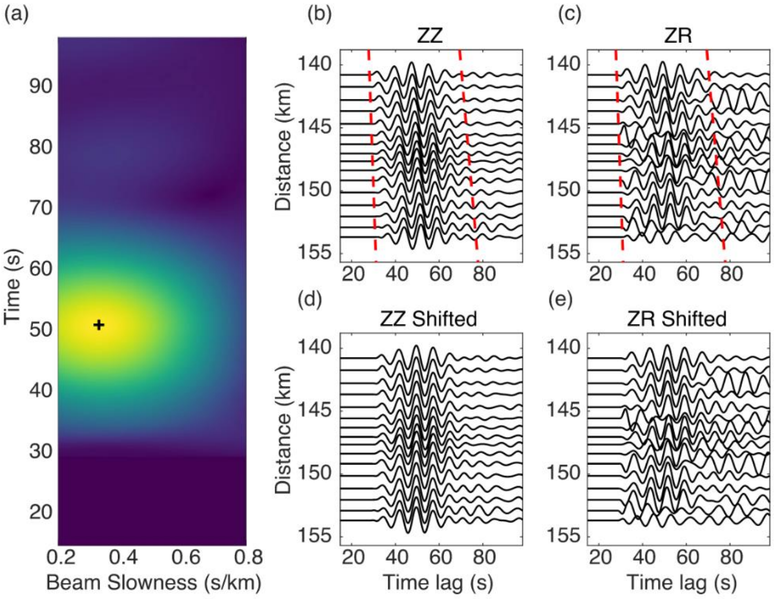

Figure 3. Example calculation of phase slowness based on slant stacking using the southernmost node as a source and beam 54 as a receiver (Figure 1). (a) Amplitude as a function of time and phase slowness of the shifted and stacked waveform envelope; the cross denotes the maximum amplitude of the grid search. (b) ZZ and (c) ZR component waveform before shifting; the red dashed lines denote reference velocity of 2 and 5 km/s (d) ZZ and (e) ZR component waveforms shifted by the maximum amplitude slowness.

In this procedure, only the correlation time lag corresponding to north propagation waves (the dominant noise direction) is used. A plane wave propagating in the great circle direction is assumed when calculating the shift time (Y. Wang, Allam, & Lin, 2019; Y. Wang, Lin, & Ward, 2019). To satisfy the far-field approximation, we only include cross-correlations with a distance larger than one wavelength (Liu et al., 2021), where the wavelength is estimated using a reference velocity of 4 km/s. While a stricter far-field criterion is sometimes desirable (e.g., three wavelengths; Lin et al., 2008), the one wavelength criterion used in this study is empirically determined to balance the number of measurements and the measurement uncertainty. To only keep the high-quality measurements, we further require a signal-to-noise ratio (SNR) greater than 5 on the stacked ZZ correlogram. The SNR is calculated based on the ratio between peak amplitude within the signal window (velocity between 1.5 and 5 km/s)

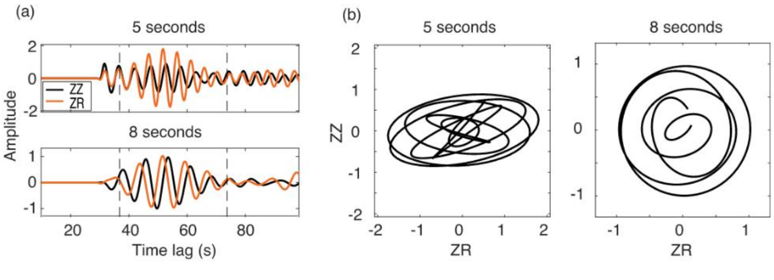

Figure 4. (a) ZZ (black) and ZR (orange) waveforms for (top) 5 s and (bottom) 8 s for the same source and receiver as in Figure 3. (b) Particle motion for waveforms in the left panel. For this example, the *H*/*V* measurements are 1.81 (5 s) and 1.03 (8 s).

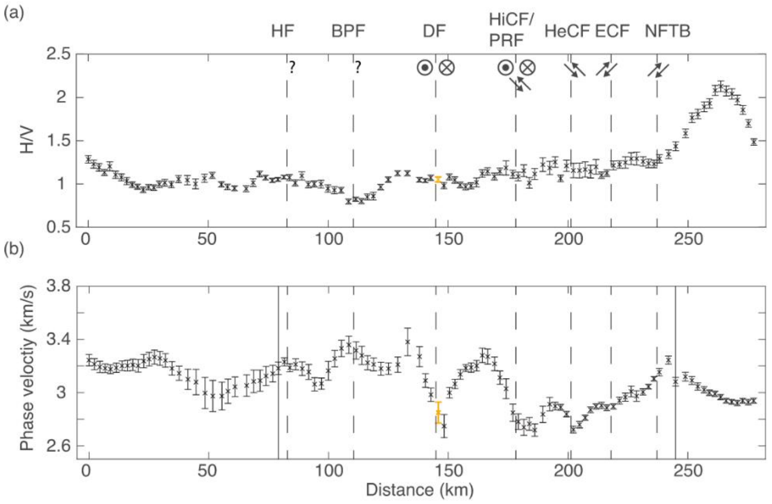

Figure 5. (a) *H*/*V* and (b) phase velocity measurements across the arrays at 8 s period. Error bars represent the uncertainties or standard deviation of the mean. Dashed lines represent the surface trace of the faults (Figure 1), solid lines represent the change from 30 km beams to 15 km beams, with 15 km beams used between about 63.0 and 64.25 latitude. The distance is a cumulative segmented distance connecting the 106 beams, starting with Beam 1 at 0 km in the south (Figure 1b). The orange measurement (Figure 1) and its uncertainty is the location—very close to the Denali fault—used as an example in Figures 7 and 8.

and root-mean-square (RMS) noise amplitude within the noise window, which is assigned as the end of the signal window to 20 s before the end of the correlogram.

The receiver beam phase slowness resolved using the ZZ component is then applied to also shift and stack the ZR waveforms. We use the ratio of the stacked ZZ and ZR maximum envelope amplitudes to determine the receiver beam Rayleigh wave *H*/*V* ratios (Figure 4). While *H*/*V* ratios can in principle also be measured using RZ and RR cross-correlations (Berg et al., 2018; Lin et al., 2014), these are not considered in this study because the RR cross-correlations are much noisier. In addition to requiring the SNR >5 for both stacked ZZ and ZR correlograms, two additional quality control criteria are used to remove less reliable *H*/*V* ratio measurements. First, we require that the ZZ and ZR phase travel time difference is smaller than one-eighth of a period, after accounting for the expected 90-degree phase shift (one-fourth of a period) between the vertical and radial components. Second, we require the ZZ and ZR group travel time difference to be smaller than one period to ensure we are measuring the same energy package for the two components.

For each receiver beam center location and each period, we determine the local Rayleigh wave phase slowness and *H*/*V* ratio and their uncertainties based on the mean and the standard deviation of the mean of all available measurements with different source stations. To remove outliers, we discard all measurements more than two standard deviations away from the mean and we also discard beams with less than 10 measurements in total. Figure 5 shows the resulting phase velocity and *H*/*V* ratio profiles across the entire linear array for 8 s period. The distance is measured along a segmented profile connecting each beam centers from south to north; it does not represent a cross-section along a great circle. For example, the end-to-end distance of 270 km is less than the along-road distance of 306 km between the most distant nodes. There are two reasons for this. First, the southernmost and northernmost beam centers are 8 km north and south of the southernmost and the northernmost node. The second reason is that simplifying the road geometry from 306 nodes to 106 beams can result in a loss of intricate curves and bends. Figure 6 summarizes the results for all periods and the corresponding uncertainty, where white patches represent situations where insufficient measurements (<10) passed the selection criteria imposed.

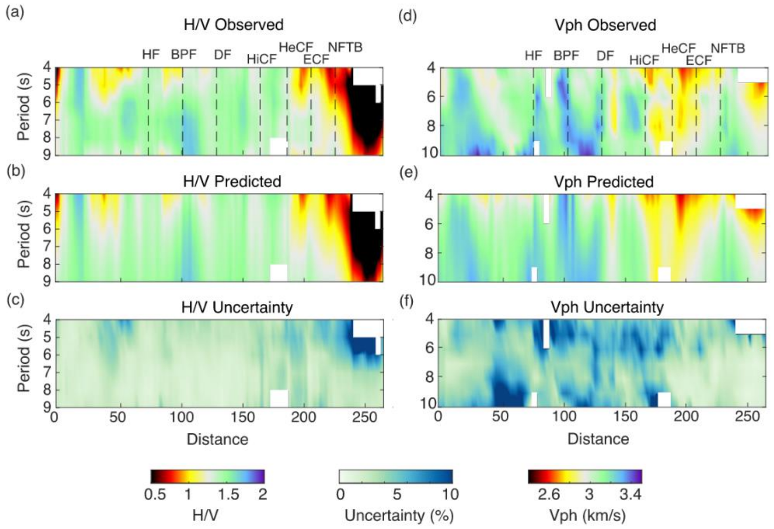

Figure 6. Measured *H*/*V* (a) and phase velocity (d). Predicted *H*/*V* (b) and phase velocity (e). Uncertainty of *H*/*V* (c) and phase velocity (f). These measurements are used in combination with the depth sensitivity functions in Figure 8 to generate the 2D V_s models in Figure 9. The fault abbreviations are identified in Figure 1.

2.4. MCMC Joint Inversion

We jointly invert Rayleigh wave phase dispersion and *H*/*V* ratio measurements at each location using a 1-D Markov Chain Monte Carlo (MCMC) method to resolve shear wave velocity (V_s) structure in the crust (Figure 7; Berg et al., 2020; Liu et al., 2021; Shen & Ritzwoller, 2016). The complementary sensitivity of Rayleigh wave phase velocities and *H*/*V* ratios (Figure 8) allows the crustal structure to be resolved from the surface to 16 km. We parametrize the V_s model to include a linearly increasing sedimentary layer (0–4 km thickness) and with the rest of the crust (down to 30 km) described by four cubic B-splines (Table 1). We use the Brocher (2005) empirical relationships to determine V_p and densities based on V_s. We use a 1-D V_s model extracted from a global V_s model (Shapiro & Ritzwoller, 2002) as the starting reference model of the inversion.

To fully explore the model space, we allow the MCMC inversion to search for V_s velocities that are up to ±3 km/s from the reference model. Two constraints are imposed to avoid unrealistic Earth models: (a) the V_s in the crust cannot be larger than 4.9 km/s, and (b) we require a positive jump in velocity at the base of the linear sedimentary layer. For each 1D inversion, we compute 3,000 randomly generated iterations with 12 jumps, generate more than 30,000 models, and accept only models within 1.5 times the minimum misfit. We average all the accepted models to obtain the final averaged model (Figure 7a). Only the top 16 km of the model is considered robust based on the sensitivity kernels of 4–10 s period Rayleigh wave measurements (Figure 8). All the piecewise continuous 1-D models are connected to construct the final 2-D V_s model across the array (Figure 9).

3. Results

3.1. Ellipticity and Phase Velocity Results

The resulting phase velocity profile (Figure 6d) reveals HiCF/PRF as an apparent boundary between faster velocities in the south and slower velocities in the north. The faster velocities in the south are mostly continuous in the 8–10 s range, sensitive to structure in the middle crust (Figure 8b), where small-scale variations between 3.0 and 3.4 km/s are observed for shorter periods. The DF emerges as a prominent localized low-velocity anomaly down to ~8 s period. For the northern half of the profile, there are three distinct short-period low-velocity anomalies: centered at the HiCF/PRF, bounded by the Healy Creek Fault (HeCF) and the Ealy Creek fault (ECF), and north

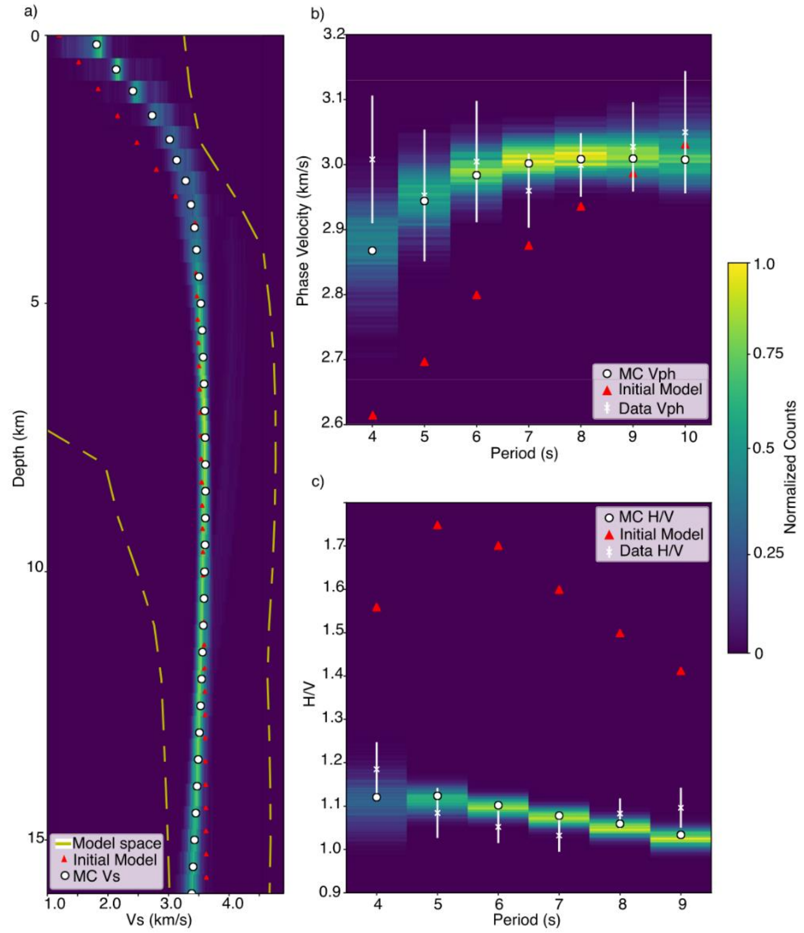

Figure 7. Example of Markov Chain Monte Carlo joint inversion for a 1-D V_s model at a location close to the Denali fault (Figure 5, orange marker), with 4410 models accepted. (a) Shear wave velocity versus depth showing the initial model (red triangles), the model space (dashed yellow lines), posterior model density (background color), and final mean model (white dots). (b) Rayleigh wave phase velocity dispersion measurements with its uncertainties from this study (white crosses with error bars) and predicted dispersion curves from the starting model (red triangles), posterior model density (background color), and final mean model (white dots). (c) Same as panel (b) but for Rayleigh *H*/*V* ratios.

of the Northern Foothills Thrust Belt (NFTB). The uncertainty on the measurements shows larger uncertainties for shorter periods (4–6 s) than for longer periods (7–10 s), likely due to stronger heterogeneity and wavefield complexity, such as multipathing or scattering. However, most uncertainties of the measurements are below 5%.

The resulting *H*/*V* ratio profile (Figure 6a) reveals structures distinct from the phase velocity profile, as *H*/*V* ratios are most sensitive to shallow crustal structure (Figure 8a; Lin et al., 2012). The observation of a high and low *H*/*V* ratio represents a large and small shallow velocity contrast/gradient, respectively, common for sedimentary basins and mountain ranges. There are several areas of high *H*/*V* ratios in the resulting profile. The highest *H*/*V* ratios are measured in the northern end of the array, bounded by the NFTB in the south. South of the NFTB and north of the HeCF, there are two different high *H*/*V* areas separated by the ECF. The other high *H*/*V* area is near the southern end of the profile. Unlike the phase velocity profile, we see no evidence of major fault zones in our

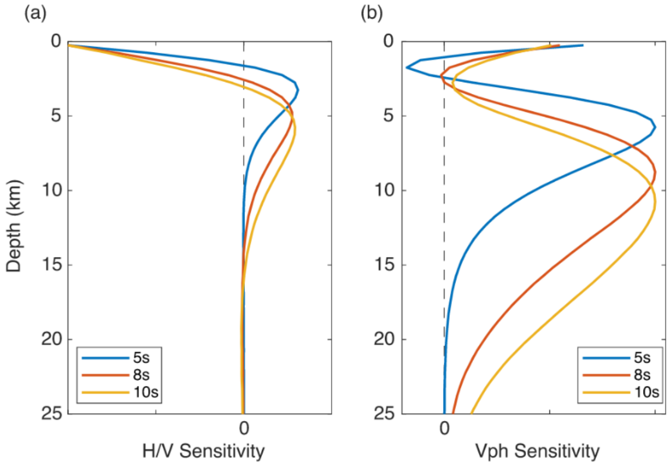

Figure 8. Example sensitivity kernels to changes in V_s at depth. (a) *H*/*V* and (b) phase velocity sensitivity kernels for a location near the Denali fault (Figure 5, orange marker) at three different periods calculated based on the inverted shear-wave velocity model.

ellipticity measurements. Besides elevated uncertainties near the northern edge coinciding with the higher *H*/*V* ratios, the *H*/*V* measurements mostly have uncertainty values below 5%.

3.2. Shear Wave Velocity Model

The shallow and deeper structures of the inverted shear velocity model (Figures 9a and 9b), in general, agree well with the pattern of the input *H*/*V* ratio and phase velocity profiles, with the predicted phase velocity and *H*/*V* ratio profiles in good agreement with the observed profiles (Figure 6). In the uppermost crust, major sedimentary structures with $V_s < 1.8$ km/s are observed, including the Susitna basin (SB)/Broad Pass (Figure 1) in the south, the Northern flank of the Alaska Range, and the Tanana basin (TB) in the north. Susitna basin is a Holocene basin connecting to the narrow Broad Pass and bounded by DF to the north. The Broad Pass slow anomaly is segregated by the inferred Hurricane fault (HF) and Broad Pass fault (BPF) locations. The Northern flank of the Alaska Range is the wedge-top depozone of the NFTB (Ridgway et al., 2007), and the slow anomaly is bounded and segregated by HeCF, ECF, and NFTB. North of NFTB, extremely slow V_s velocity (<1 km/s) is observed within the TB, which is a continental foreland basin covered by Holocene alluvial, fluvial, and lacustrine deposits.

Table 1
Prior Distributions in Joint Inversion

Parameters	Range
Sedimentary layer thickness	2 ± 2*m*0 (km)
Sedimentary layer Vsv (top and bottom)	*m*0 ± 3.0 (km/s)
Crust b-spline coefficients (4 total)	*m*0 ± 3.0 (km/s)

Note. All parameters (left column), (right column) the ranges explored with *m*0 corresponding to the starting model variable's associated value.

Few major surface fault traces appear to extend deeper down and correlate with deeper crustal V_s structure (Figure 9b). Between 8 and 16 km depth, crustal velocity is generally slower north of the HiCF/PRF, presumably corresponding to the pericratonic YCT. A prominent low V_s anomaly (<3.2 km/s) bounded by HiCF/PRF and ECF is observed, which trends shallower around HeCF beneath Jumbo Dome (JB) and BC volcanic structure. The location of this slow anomaly also coincides with where the subducted Pacific-Yakutat slab steepened and deepened below 100 km depth (Figure 9d; Hayes et al., 2018). The overall faster structure south of HiCF/PRF is corresponding to the heterogenous SZ. The DF emerged as a narrow vertical slow anomaly down to ~12 km depth. A sharp velocity change is observed across the BPF although the nature of the velocity contrast is not so clear.

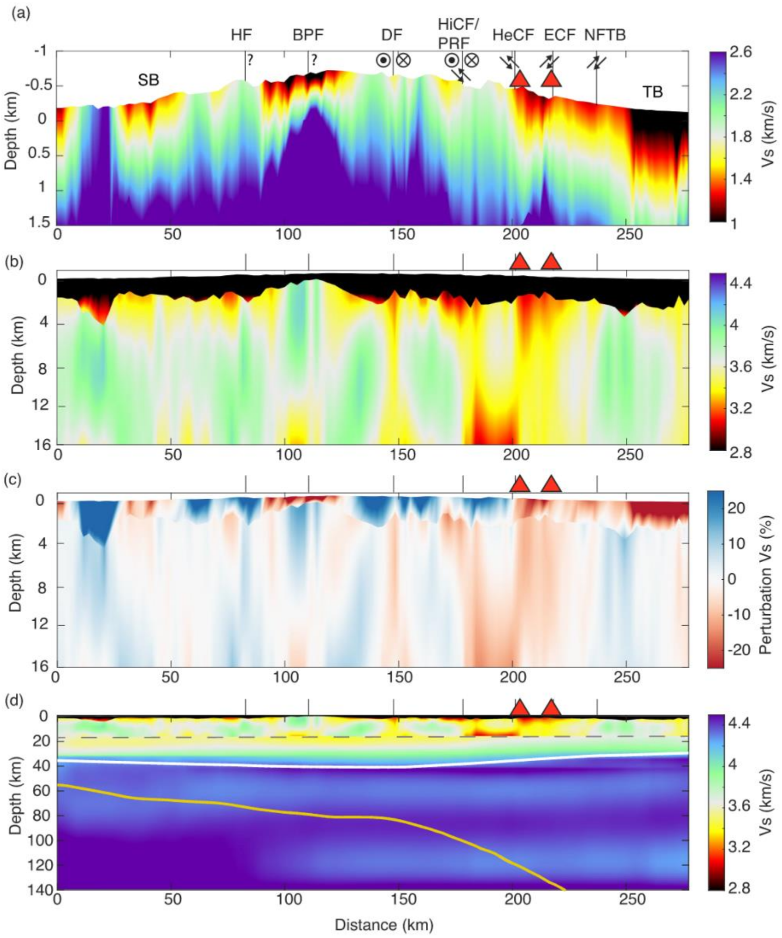

Figure 9. The inverted shear velocity (V_s, km/s) model. (a) Depth 0–1.5 km; vertical exaggeration 90×. (b) Depth 0–16 km; vertical exaggeration 15×. The locations of Susitna basin and Tanana basin are identified. Panel (c) same as panel (b) but for the V_s perturbation relative to the depth-averaged velocity. (d) The shear velocity model of this study (top 16 km above the dashed line and of Berg et al. (2020), 16–150 km). The white line is the Moho depth estimations from Miller & Moresi, 2018, and the yellow line is the depth of the slab from Slab 2.0 (Hayes et al., 2018); vertical exaggeration 2×. The fault abbreviations are identified in Figure 1.

4. Discussion

4.1. Magmatic Material Beneath the DVG

The low-velocity anomaly we observe beneath ~12 km depth between the HiCF/PRF and the ECF has not been previously reported either in regional studies (A. A. Allam et al., 2017; Eberhart-Phillips et al., 2006; Rondenay et al., 2010; Y. Wang & Tape, 2014; X. Yang & Gao, 2020) or in recent continental studies (Berg et al., 2020; Martin-Short et al., 2018; Ward & Lin, 2018). In the upper crust, this area, part of the DVG, contains the Northern Foothills fold-and-thrust belt that propagates northward. The interpreted location of the basal detachment of the fold-and-thrust belt here is around 7–8 km depth (Bemis & Wallace, 2007), right above the top of the observed low-velocity anomaly. There are a few mechanisms that can result in an anomalous mid-crust low-velocity body, such as mineral composition, temperature, pressure, crack density, fluid content, or a combination of those factors.

First, the low-velocity anomaly might be related to fluids, either melt or fluid-filled cracks. The presence of the BC and Jumbo Dome could suggest that the slow velocity anomaly is related to magmatic/partial melt material rising from below and accumulating in the middle crust. Assuming V_s of 3.8 km/s (above the slow velocity zone) for the host rock, a ∼15% melt percentage will be needed to reduce the V_s to ∼3.2 km/s in the low-velocity zone, based on the modeling of preferred crystallographic orientation (Lee et al., 2017). Second, the low-velocity anomaly might correspond to a compositional change. North of the DF, the composition of the crust is mainly metasedimentary and metavolcanic rocks (Jones et al., 1983). Brennan et al. (2011) observed a negative anomaly in the receiver function and calculated a velocity ratio between *P*-wave and *S*-wave of ∼1.6 for the area. The low ratio led to an interpretation of a crust with felsic composition and a juxtaposition of metamorphic rocks (greenschist over amphibolite), which Pavlis et al. (1993) suggest requires eliminating 10 km of the crustal column. Nevertheless, subsequent studies calculating V_p, V_s, and V_p/V_s have not observed this low ratio in the area, and they report a ratio higher than 1.75 (A. A. Allam et al., 2017). A negative receiver function anomaly from local models (A. A. Allam et al., 2017; Brennan et al., 2011) and a higher V_p/V_s (A. A. Allam et al., 2017) would favor the explanation of the low-velocity anomaly as fluid related instead of compositionally related. The geophysical data do not allow us to distinguish the type of fluids present in the low-velocity anomaly.

Although we do not have the sensitivity to resolve the lower crust and the upper mantle, our observation and the presence of recent basaltic volcanic activity (∼10 ka) indicate that the mantle below the DVG is generating melt, and the material is reaching the surface. Our observation suggests that the magmatic material reaches the mid-crust beneath the northern flank of the Alaska Range, and it is stored around 12 km deep. We infer that the upward migration of the material is probably inhibited by the compressive stress from the shortening of the plate boundary transferred north of the DF to the fold-thrust belt, possibly sealing pathways in the crust, thereby hindering the movement of molten magma toward the surface (Bemis et al., 2015; McNamara & Pasayanos, 2002). Sporadically, the material may travel up to the detachment zone of the fold-thrust belt (Bemis & Wallace, 2007) and subsequently reach the surface through weak zones resulting from the fold and thrust system in the northern foothills of the Alaska Range.

4.2. Denali Fault and Other Faults

The DF is imaged in our results as a narrow, low-velocity zone at the same location as the surface trace of the fault (Figure 9b). Low-velocity zones are a common feature of seismogenic faults. They are created by breaking surrounding rock during coseismic shaking (Ben-Zion & Sammis, 2003). The velocity reduction at 3.5–10 km depth is around 15% from the surrounding crust. The narrow zone widens at depth (10–16 km) to the north. This type of geometry has been modeled for strike-slip faults (Finzi et al., 2009). In the 0–3.5 km depth range, the velocity is also slightly lower in the immediate vicinity of the DF compared to the surrounding structure, which could be related to the fault damage zone. Previous geophysical observations in the Eastern DF reported a maximum of 5 km wide composite damage zone attributed to the presence of several fault strands in a narrow area (Brocher et al., 2004) and geological observations indicate that the surface trace of the fault is in some locations <200 m wide (Benowitz et al., 2022). A damage zone structure typically ranges in size from hundreds of meters (Faulkner et al., 2011), to faults with damage zones that extend up to 1.5 km in width (Cochran et al., 2009). We cannot resolve smaller-scale structures (<5 km), given the limits on the resolution imposed by the beam size and the wavelength of the surface waves used in this research. The minimum resolution for this study, from ray theory, is half of the wavelength for each period (Z. Wang & Dahlen, 1995; Y. Wang, Allam, & Lin, 2019).

None of the other faults on this transect show a distinct fault zone structure near the surface (<1.5 km) or in the shallow- to mid-crust (1.5–16 km). There are two potential reasons for this. First, the previously discussed limitations on resolution could be a factor. Second, the presence of geological or tectonic boundaries associated with faults in the area could play a role. Larger velocity contrasts between different rock types may mask signals from smaller anomalies, in this case, a fault damage zone.

4.3. Suture Zone Northern Limit With the Yukon Terrane Boundary

We interpret the 10%–15% change of velocity at the HiCF/PRF as the northern edge of the SZ and the crustal boundary between the seismically faster SZ and the seismically slower YCT in the north (Figures 9b and 9c). The differences in seismic velocity between the north and the south can be explained by the geological history and the compositional change from oceanic to continental affinity crust from south to north (Hampton et al., 2010; Plafker & Berg, 1994; Ridgway et al., 2002). Our geophysical observation agrees with geological mapping interpreting the HiCF as the northern boundary of the SZ (Ridgway et al., 2002; Wahrhaftig et al., 1975). It would also agree with deeper observations of a sharp contrast in the Moho in the HiCF (Brennan et al., 2011; Miller & Moresi, 2018; Veenstra et al., 2006). Although it contrasts with previous local earthquake tomography results that identified the DF as the boundary of the SZ (A. A. Allam et al., 2017).

The fast velocity area bounded by the BPF to the north and the HF to the south could be related to the mafic and ultramafic rocks of the BPT underlining the Chulitna terrane (Jones et al., 1980) and corresponds with a positive magnetic anomaly (Burns et al., 2020). The BPF and the HF played an important role during the formation of the SZ in the Late Cretaceous with inferred strike-slip or thrust displacements (Clautice, Newberry, Blodgett, et al., 2001; Clautice, Newberry, Pinney, et al., 2001; Jones et al., 1980). They have been reactivated during the Holocene with a few kilometers of thrust displacement (Haeussler, Saltus, et al., 2017). The relationship between the terranes and the faults in the Broad Pass area is not fully understood (Clautice, Newberry, Blodgett, et al., 2001; Clautice, Newberry, Pinney, et al., 2001).

4.4. Sedimentary Basins

Our profile is bounded by two sedimentary basins: SB in the south and TB in the north. The southernmost low-velocity zone is located north of the main depocenter of SB, where exploration wells and seismic reflection lines show a sedimentary thickness of 4.5–5 km (Lewis et al., 2015; B. R. G. Stanley et al., 2013; R. G. Stanley et al., 2014). The geometry and depth of the observed low-velocity anomaly suggest an independent accumulation zone on the northern edge of the basin (Figures 9a and 9b). Sediment thickness information in the Broad Pass along the Chulitna River is scarce. The two low-velocity zones observed near the BPF (Figure 9a) agree with two distinct negative Bouguer gravity anomalies in the area (Meyer, 2005).

Our observation of thinning of the sedimentary layers from the HiCF/PRF toward the NFTB has also been reported using topography and structural geology observations (Bemis & Wallace, 2007). The low-velocity zones along the northern flank of the Alaska Range (Figures 9a and 9b) have been referred to as the wedge-top depozone of the TB in the fold and thrust system deformation (Ridgway et al., 2007). We identify two distinct anomalies in the Alaska Range. The southernmost anomaly, which we interpret as the foredeep basin (Ridgway et al., 2007), is deeper and has slower velocities at depth compared to the northern anomaly, which we interpret as the forebulge extending toward the Yukon-Tanana Uplands. In the northernmost anomaly, we observe a layer of 700–800 m with velocities lower than 1 km/s, and we observe velocities lower than 3 km/s up to 2.5–3 km depth.

Previous studies on the TB report depths of 1.5 km to the basement (Dixit & Hanks, 2021; Trop & Ridgway, 2007). The high velocity in the basement can be explained by the Yukon–Tanana Terrane schist underlying the basin (Dixit & Hanks, 2021). Our profile (Figure 1b) does not extend north beyond the town of Nenana into the Nenana basin (NB), where sediments up to 8 km deep have been interpreted from borehole data and seismic reflection data in the NB (Dixit & Hanks, 2021; Van Kooten et al., 2012).

5. Conclusions

This study presents a high-resolution 2-D shear-wave velocity profile of south-central Alaska across the DF and the Alaska Range. We measure Rayleigh wave H/V ratios and phase velocities calculated from ambient noise cross-correlation and invert for a shear velocity model through a joint MCMC inversion, which takes advantage of the complementary sensitivities of the measurements. We observe a mid-crust, low-velocity anomaly north of the HiCF and south of the Buzzard Creek and Jumbo Dome volcanoes. We favor the scenario that the LVZ is formed by fluids or melt material generated by the subducted slab being stored in the mid-crust. Within the top 5 km, our model delineates the SB, and the TB, south and north of the Alaska Range, respectively. We imaged the Alaska SZ in detail, including the northern limit at the HiCF, where seismic velocity in the north drops around 10%–15%.

We also imaged the DF as a narrow low-velocity anomaly extending to depths of 10–12 km. The new observation of the low-velocity anomaly beneath the DVG should spark future research to assess any possible hazard and to image the lateral limits of the anomaly. The use of other seismic and geophysical techniques with additional seismic deployments can help to measure the 3D extent and nature of the LVZ and is the target of future work.

Data Availability Statement

Data processing was performed with Seismic Analysis Code (SAC) and Matlab. Figure generation was performed in Matlab and Python 3.8. The nodal data is available on the Incorporated Research Institutions for Seismology (IRIS) database with DOI A. Allam et al. (2019) (https://doi.org/10.7914/SN/ZE_2019). Additional seismic data included broadband stations from the Alaska Earthquake Center (1987) (DOI: https://doi.org/10.7914/SN/AK), the Earthscope Transportable Array (2003) (DOI: https://doi.org/10.7914/SN/TA) and the FLATS array (Tape & West, 2014) (DOI: https://doi.org/10.7914/SN/XV_2014). The 2-D shear wave velocity model is available at https://doi.org/10.5281/zenodo.10257242.

Acknowledgments
This study was supported by the National Science Foundation (NSF) Grant EAR 1753362 (Lin), 1736248 (Allam), 1736223 (Tape), 1917482 (Tape), 1917446 (Allam), and 1917368 (Ward). S. R. acknowledges a scholarship by the *Consejo Nacional de Ciencia y Tecnología* (CONACYT; Scholarship number: 710069). We are grateful to the numerous students and volunteers who helped deploy and recover the instruments. We would also like to acknowledge PASSCAL and Incorporated Research Institutions for Seismology (IRIS) DMC for their help with the deployment, recovery, and data archiving.

References

Alaska Earthquake Center, University of Alaska Fairbanks. (1987). Alaska regional network [Dataset]. International Federation of Digital Seismograph Networks. https://doi.org/10.7914/SN/AK

Albanese, M. (1980). *The geology of three extrusive bodies in central Alaska Range* (Master thesis). University of Alaska Fairbanks.

Allam, A., Tape, C., & Ward, K. (2019). Node deployment along the intersection of the Denali Fault and Parks Highway [Dataset]. International Federation of Digital Seismograph Networks. https://doi.org/10.7914/SN/ZE_2019

Allam, A. A., Schulte-Pelkum, V., Ben-Zion, Y., Tape, C., Ruppert, N., & Ross, Z. E. (2017). Ten kilometer vertical Moho offset and shallow velocity contrast along the Denali fault zone from double-difference tomography, receiver functions, and fault zone head waves. In *Tectonophysics* (Vol. 721, pp. 56–69). Elsevier BV. https://doi.org/10.1016/j.tecto.2017.09.003

Andronikov, A. V., & Mukasa, S. B. (2010). 40Ar/39Ar eruption ages and geochemical characteristics of Late Tertiary to Quaternary intraplate and arc-related lavas in interior Alaska. *Lithos*, *115*(1–4), 1–14. https://doi.org/10.1016/j.lithos.2009.11.002

Athey, J., Newberry, R., Werden, M., Freeman, L., Smith, R., & Szumigala, D. (2006). Bedrock geologic map of the liberty Bell area, Fairbanks A-4 Quadrangle, Bonnifield mining district, Alaska. In *Report of investigation RI2006, 1.0.1*.

Bemis, S. P., Carver, G. A., & Koehler, R. D. (2012). The Quaternary thrust system of the northern Alaska Range. *Geosphere*, *8*(1), 196–205. https://doi.org/10.1130/GES00695.1

Bemis, S. P., & Wallace, W. K. (2007). Neotectonic framework of the north-central Alaska range foothills. *Special Paper of the Geological Society of America*, *431*(21), 549–572. https://doi.org/10.1130/2007.2431(21)

Bemis, S. P., Weldon, R. J., & Carver, G. A. (2015). Slip partitioning along a continuously curved fault: Quaternary geologic controls on Denali fault system slip partitioning, growth of the Alaska Range, and the tectonics of south-central Alaska. *Lithosphere*, *7*(3), 235–246. https://doi.org/10.1130/L352.1

Benowitz, J. A., Roeske, S. M., Regan, S. P., Waldien, T. S., Elliott, J. L., & O'Sullivan, P. B. (2022). Large-scale, crustal-block vertical extrusion between the Hines Creek and Denali faults coeval with slip localization on the Denali fault since ca. 45 Ma, Hayes Range, Alaska, USA. *Geosphere*, *18*(3), 1030–1054. https://doi.org/10.1130/ges02466.1

Ben-Zion, Y., & Sammis, C. G. (2003). Characterization of fault zones. *Pure and Applied Geophysics*, *160*(3), 677–715. https://doi.org/10.1007/PL00012554

Berg, E. M., Lin, F., Allam, A., Schulte-Pelkum, V., Ward, K. M., & Shen, W. (2020). Shear velocity model of Alaska via joint inversion of Rayleigh wave ellipticity, phase velocities, and receiver functions across the Alaska transportable array. *Journal of Geophysical Research: Solid Earth*, *125*(2), 1–22. https://doi.org/10.1029/2019JB018582

Berg, E. M., Lin, F. C., Allam, A., Qiu, H., Shen, W., & Ben-Zion, Y. (2018). Tomography of southern California via Bayesian joint inversion of Rayleigh wave ellipticity and phase velocity from ambient noise cross-correlations. *Journal of Geophysical Research: Solid Earth*, *123*(11), 9933–9949. https://doi.org/10.1029/2018JB016269

Brennan, P. R., Gilbert, H., & Ridgway, K. D. (2011). Crustal structure across the central Alaska Range: Anatomy of a Mesozoic collisional zone. *Geochemistry, Geophysics, Geosystems*, *12*(4), 52. https://doi.org/10.1029/2011GC003519

Brocher, T. M. (2005). Empirical relations between elastic wavespeeds and density in the Earth's crust. *Bulletin of the Seismological Society of America*, *95*(6), 2081–2092. https://doi.org/10.1785/0120050077

Brocher, T. M., Fuis, G. S., Lutter, W. J., Christensen, N. I., & Ratchkovski, N. A. (2004). Seismic velocity models for the Denali fault zone along the Richardson Highway, Alaska. *Bulletin of the Seismological Society of America*, *94*(6B), S85–S106. https://doi.org/10.1785/0120040615

Brueseke, M. E., Benowitz, J. A., Trop, J. M., Davis, K. N., Berkelhammer, S. E., Layer, P. W., & Morter, B. K. (2019). The Alaska Wrangell Arc:∼ 30 Ma of subduction-related magmatism along a still active arc-transform junction. *Terra Nova*, *31*(1), 59–66. https://doi.org/10.1111/ter.12369

Burns, L. E., Graham, G. R. C., Barefoot, J. D., Woods, R.-E., & Pritchard, R. A. (2020). *Chulitna electromagnetic and magnetic airborne geophysical survey*. Alaska Division of Geological & Geophysical Surveys. https://doi.org/10.14509/30416

Cameron, C. E., Nye, C. J., Bull, K. F., & Woods, R.-E. (2015). *Jumbo Dome, Interior Alaska: Whole-rock, major- and trace-element analyses*. State of Alaska, Department of Natural Resources, Division of Geological & Geophysical Surveys. https://doi.org/10.14509/29520

Chuang, L., Bostock, M., Wech, A., & Plourde, A. (2017). Plateau subduction, intraslab seismicity, and the Denali (Alaska) volcanic gap. *Geology*, *45*(7), 647–650. https://doi.org/10.1130/G38867.1

Clautice, K. H., Newberry, R. J., Blodgett, R. B., Bundtzen, T. K., Gage, B. G., Harris, E. E., et al. (2001). *Bedrock geologic map of the Chulitna region, southcentral Alaska*. Alaska Division of Geological & Geophysical Surveys. https://doi.org/10.14509/2768

Clautice, K. H., Newberry, R. J., Pinney, D. S., Blodgett, R. B., Bundtzen, T. K., Gage, B. G., et al. (2001). *Geologic map of the Chulitna region, southcentral Alaska*. Alaska Division of Geological & Geophysical Surveys. https://doi.org/10.14509/2771

Cochran, E. S., Li, Y. G., Shearer, P. M., Barbot, S., Fialko, Y., & Vidale, J. E. (2009). Seismic and geodetic evidence for extensive, long-lived fault damage zones. *Geology*, *37*(4), 315–318. https://doi.org/10.1130/G25306A.1

Dixit, N. C., & Hanks, C. (2021). Basement structure and styles of active tectonic deformation in central interior Alaska. *Geosciences*, *11*(3), 1–28. https://doi.org/10.3390/geosciences11030127

Earthscope Transportable Array. (2003). USArray transportable array [Dataset]. International Federation of Digital Seismograph Networks. https://doi.org/10.7914/SN/TA

Eberhart-Phillips, D., Christensen, D. H., Brocher, T. M., Hansen, R., Ruppert, N. A., Haeussler, P. J., & Abers, G. A. (2006). Imaging the transition from Aleutian subduction to Yakutat collision in central Alaska, with local earthquakes and active source data. *Journal of Geophysical Research*, *111*(B11), B11303. https://doi.org/10.1029/2005JB004240

Faulkner, D. R., Mitchell, T. M., Jensen, E., & Cembrano, J. (2011). Scaling of fault damage zones with displacement and the implications for fault growth processes. *Journal of Geophysical Research*, *116*(B5), B05403. https://doi.org/10.1029/2010JB007788

Finzi, Y., Hearn, E. H., Ben-Zion, Y., & Lyakhovsky, V. (2009). Structural properties and deformation patterns of evolving strike-slip faults: Numerical simulations incorporating damage rheology. *Pure and Applied Geophysics*, *166*(10), 1537–1573. https://doi.org/10.1007/s00024-009-0522-1

Freymueller, J. T., Woodard, H., Cohen, S. C., Cross, R., Elliott, J., Larsen, C. F., et al. (2008). Active deformation processes in Alaska, based on 15 years of GPS measurements. In J. T. Freymueller, P. J. Haeussler, R. L. Wesson, & G. Ekström (Eds.), *Active tectonics and seismic potential of Alaska*. https://doi.org/10.1029/179GM02

Gutscher, M. A., Maury, R., Eissen, J. P., & Bourdon, E. (2000). Can slab melting be caused by flat subduction? *Geology*, *28*(6), 535–538. https://doi.org/10.1130/0091-7613(2000)28<535:CSMBCB>2.0.CO;2

Gutscher, M. A., Spakman, W., Bijwaard, H., & Engdahl, E. R. (2000). Geodynamics of flat subduction: Seismicity and tomographic constraints from the Andean margin. *Tectonics*, *19*(5), 814–833. https://doi.org/10.1029/1999TC001152

Haeussler, P. J. (2008). An overview of the neotectonics of interior Alaska: Far-field deformation from the Yakutat microplate collision. In J. T. Freymueller, P. J. Haeussler, R. L. Wesson, & G. Ekström (Eds.), *Active tectonics and seismic potential of Alaska*. https://doi.org/10.1029/179GM05

Haeussler, P. J., Matmon, A., Schwartz, D. P., & Seitz, G. G. (2017). Neotectonics of interior Alaska and the late Quaternary slip rate along the Denali fault system. *Geosphere*, *13*(5), 1445–1463. https://doi.org/10.1130/GES01447.1

Haeussler, P. J., Saltus, R. W., Stanley, R. G., Ruppert, N., Lewis, K., Karl, S. M., & Bender, A. (2017). The Peters Hills basin, a Neogene wedge-top basin on the Broad Pass thrust fault, south-central Alaska. *Geosphere*, *13*(5), 1464–1488. https://doi.org/10.1130/ges01487.1

Hampton, B. A., Ridgway, K. D., & Gehrels, G. E. (2010). A detrital record of Mesozoic island arc accretion and exhumation in the North American Cordillera: U-Pb geochronology of the Kahiltna basin, southern Alaska. *Tectonics*, *29*(4), TC4015. https://doi.org/10.1029/2009TC002544

Hayes, G. P., Moore, G. L., Portner, D. E., Hearne, M., Flamme, H., Furtney, M., & Smoczyk, G. M. (2018). Slab2, a comprehensive subduction zone geometry model. *Science*, *362*(6410), 58–61. https://doi.org/10.1126/science.aat4723

Jones, D. L., Silberling, N. J., Csejtey, B., Jr., Nelson, W. H., & Blome, C. D. (1980). Age and structural significance of ophiolite and adjoining rocks in the upper Chulitna district, south-central Alaska: US Geol. In *Survey professional paper* (p. 1121).

Jones, D. L., Silberling, N. J., Gilbert, W. J., & Coney, P. J. (1983). Tectono-stratigraphic map and interpretive bedrock geologic map of the Mount McKinley region, Alaska (no. 83-11).

Koehler, R. D., Burns, P. A. C., & Weakland, J. R. (2013). Digitized faults of the Neotectonic map of Alaska (Plafker and others, 1994). In R. D. Koehler (Ed.), *Quaternary faults and folds (QFF)* (Vol. 150, p. 1). Alaska Division of Geological & Geophysical Surveys Miscellaneous Publication. https://doi.org/10.14509/24791

Koehler, R. D., Farrell, R.-E., Burns, P. A. C., & Combellick, R. A. (2012). Quaternary faults and folds in Alaska: A digital database. In R. D. Koehler (Ed.), *Quaternary faults and folds (QFF), 1 sheet, scale 1:3,700,000* (Vol. 141, p. 31). Alaska Division of Geological & Geophysical Surveys Miscellaneous Publication. https://doi.org/10.14509/23944

Lee, A. L., Walker, A. M., Lloyd, G. E., & Torvela, T. (2017). Modeling the impact of melt on seismic properties during mountain building. *Geochemistry, Geophysics, Geosystems*, *18*(3), 1090–1110. https://doi.org/10.1002/2016GC006705

Lewis, K. A., Potter, C. J., Shah, A. K., Stanley, R. G., Haeussler, P. J., & Saltus, R. W. (2015). *Preliminary interpretation of industry two-dimensional seismic data from Susitna basin, south-central Alaska*. US Department of the Interior, US Geological Survey. https://doi.org/10.3133/ofr20151138

Lin, F.-C., Moschetti, M. P., & Ritzwoller, M. H. (2008). Surface wave tomography of the western United States from ambient seismic noise: Rayleigh and love wave phase velocity maps. *Geophysical Journal International*, *173*(1), 281–298. https://doi.org/10.1111/j.1365-246X.2008.03720.x

Lin, F.-C., Schmandt, B., & Tsai, V. C. (2012). Joint inversion of Rayleigh wave phase velocity and ellipticity using USArray: Constraining velocity and density structure in the upper crust. *Geophysical Research Letters*, *39*(12), L12303. https://doi.org/10.1029/2012GL052196

Lin, F. C., Tsai, V. C., & Schmandt, B. (2014). 3-D crustal structure of the western United States: Application of Rayleigh-wave ellipticity extracted from noise cross-correlations. *Geophysical Journal International*, *198*(2), 656–670. https://doi.org/10.1093/gji/ggu160

Liu, C. N., Lin, F. C., Huang, H. H., Wang, Y., Berg, E. M., & Lin, C. H. (2021). High-resolution 3-D shear wave velocity model of northern Taiwan via Bayesian joint inversion of Rayleigh wave ellipticity and phase velocity with Formosa array. *Journal of Geophysical Research: Solid Earth*, *126*(5), 1–18. https://doi.org/10.1029/2020JB021610

Martin-Short, R., Allen, R., Bastow, I. D., Porritt, R. W., & Miller, M. S. (2018). Seismic imaging of the Alaska subduction zone: Implications for slab geometry and volcanism. *Geochemistry, Geophysics, Geosystems*, *19*(11), 4541–4560. https://doi.org/10.1029/2018GC007962

Matmon, A., Schwartz, D. P., Haeussler, P. J., Finkel, R., Lienkaemper, J. J., Stenner, H. D., & Dawson, T. E. (2006). Denali fault slip rates and Holocene–Late Pleistocene kinematics of central Alaska. *Geology*, *34*(8), 645–648. https://doi.org/10.1130/G22361.1

McNamara, D. E., & Pasayanos, M. E. (2002). Seismological evidence for a sub-volcanic arc mantle wedge beneath the Denali volcanic gap, Alaska. *Geophysical Research Letters*, *29*(16), 1814. https://doi.org/10.1029/2001GL014088

Meyer, J. F. (2005). *Principal facts for gravity data collected in the northern Susitna Basin area, southcentral Alaska*. Alaska Department of Natural Resources, Division of Geological & Geophysical Surveys. https://doi.org/10.14509/7186

Miller, M. S., & Moresi, L. (2018). Mapping the Alaskan Moho. *Seismological Research Letters*, *89*(6), 2430–2436. https://doi.org/10.1785/0220180222

Nye, C. J., Beget, J. E., Layer, P. W., Mangan, M. T., McConnell, V. S., McGimsey, R. G., et al. (2018). *Geochemistry of some quaternary lavas from the Aleutian arc and Mt. Wrangell*. Alaska Division of Geological & Geophysical Surveys. https://doi.org/10.14509/29843

Pavlis, T. L., Picornell, C., Serpa, L., Bruhn, R. L., & Plafker, G. (2004). Tectonic processes during oblique collision: Insights from the St. Elias orogen, northern North American Cordillera. *Tectonics*, *23*(3), TC3001. https://doi.org/10.1029/2003TC001557

Pavlis, T. L., Sisson, V. B., Foster, H. L., Nokleberg, W. J., & Plafker, G. (1993). Mid-cretaceous extensional tectonics of the Yukon-tanana terrane, trans-Alaska crustal transect (TACT), east-central Alaska. *Tectonics*, *12*(1), 103–122. https://doi.org/10.1029/92TC00860

Plafker, G., & Berg, H. C. (1994). Overview of the geology and tectonic evolution of Alaska. In G. Plafker & H. C. Berg (Eds.), *The geology of Alaska: Volume G-1*. Geological Society of America. https://doi.org/10.1130/DNAG-GNA-G1.989

Reger, R. D. (1980). Short notes on Alaskan geology: 1979–1980. *Angewandte Chemie International Edition*, *6*(11), 951–952. https://doi.org/10.14509/417

Ridgway, K. D., Thoms, E. E., Layer, P. W., Lesh, M. E., White, J. M., & Smith, S. V. (2007). Neogene transpressional foreland basin development on the north side of the central Alaska range, Usibelli group and Nenana gravel, Tanana Basin. *Special Paper of the Geological Society of America*, *431*(20), 507–547. https://doi.org/10.1130/2007.2431(20)

Ridgway, K. D., Trop, J. M., Nokleberg, W. J., Davidson, C. M., & Eastham, K. R. (2002). Mesozoic and Cenozoic tectonics of the eastern and central Alaska Range: Progressive basin development and deformation in a suture zone. *GSA Bulletin*, *114*(12), 1480–1504. https://doi.org/10.1130/0016-7606(2002)114<1480:MACTOT>2.0.CO;2

Romero, M. C., Ridgway, K. D., & Gehrels, G. E. (2020). Geology, U-Pb geochronology, and Hf isotope geochemistry across the Mesozoic Alaska Range suture zone (south-central Alaska): Implications for Cordilleran collisional processes and tectonic growth of North America. *Tectonics*, *39*(3), e2019TC005946. https://doi.org/10.1029/2019TC005946

Rondenay, S., Montési, L. G. J., & Abers, G. A. (2010). New geophysical insight into the origin of the Denali volcanic gap. *Geophysical Journal International*, *182*(2), 613–630. https://doi.org/10.1111/j.1365-246X.2010.04659.x

Shapiro, N. M., & Ritzwoller, M. H. (2002). Monte-Carlo inversion for a global shear-velocity model of the crust and upper mantle. *Geophysical Journal International*, *151*(1), 88–105. https://doi.org/10.1046/j.1365-246X.2002.01742.x

Shen, W., & Ritzwoller, M. H. (2016). Crustal and uppermost mantle structure beneath the United States. *Journal of Geophysical Research: Solid Earth*, *121*(6), 4306–4342. https://doi.org/10.1002/2016jb012887

Snieder, R. K. (2004). Extracting the Green's function from the correlation of coda waves: A derivation based on stationary phase. *Physical Review E*, *69*(4), 046610. https://doi.org/10.1103/PhysRevE.69.046610

Stanley, B. R. G., Haeussler, P. J., Benowitz, J. A., Goodman, D. K., Ravn, R. L., Shellenbaum, D. P., et al. (2013). New stratigraphic revelations in the subsurface Susitna basin, south-central Alaska, from recent isotopic and biostratigraphic results. In *Geological society of America abstracts with programs* (Vol. 45, p. 69). https://doi.org/10.14509/26887

Stanley, R. G., Haeussler, P. J., Benowitz, J. A., Lewis, K. A., Shellenbaum, D. P., Richard, W., et al. (2014). Tectonic implications of new geological and geophysical results from the Susitna basin, south-central Alaska. In *Search and discovery article, 10608*.

Syracuse, E. M., & Abers, G. A. (2006). Global compilation of variations in slab depth beneath arc volcanoes and implications. *Geochemistry, Geophysics, Geosystems*, *7*(5), Q05017. https://doi.org/10.1029/2005GC001045

Tape, C., Holtkamp, S., Silwal, V., Hawthorne, J., Kaneko, Y., Ampuero, J. P., et al. (2018). Earthquake nucleation and fault slip complexity in the lower crust of central Alaska. *Nature Geoscience*, *11*(7), 536–541. https://doi.org/10.1038/s41561-018-0144-2

Tape, C., & West, M. E. (2014). Fault locations and Alaska tectonics from seismicity [Dataset]. International Federation of Digital Seismograph Networks. https://doi.org/10.7914/SN/XV_2014

Trop, J. M., & Ridgway, K. D. (2007). Mesozoic and Cenozoic tectonic growth of southern Alaska: A sedimentary basin perspective. *Special Paper of the Geological Society of America*, *431*(04), 55–94. https://doi.org/10.1130/2007.2431(04)

Van Kooten, G. K., Richter, M., & Zippi, P. A. (2012). Alaska's interior rift basins: A new Frontier for discovery. *Oil and Gas Journal, Exploration and Development*. https://doi.org/10.1139/cjes-2015-0138

Veenstra, E., Christensen, D. H., Abers, G. A., & Ferris, A. (2006). Crustal thickness variation in south-central Alaska. *Geology*, *34*(9), 781–784. https://doi.org/10.1130/G22615.1

Wada, I., & Wang, K. (2009). Common depth of slab-mantle decoupling: Reconciling diversity and uniformity of subduction zones. *Geochemistry, Geophysics, Geosystems*, *10*(10), Q10009. https://doi.org/10.1029/2009GC002570

Wahrhaftig, C., Turner, D. L., Weber, F. R., & Smith, T. E. (1975). Nature and timing of movement on Hines Creek strand of Denali fault system, Alaska. *Geology*, *3*(8), 463–466. https://doi.org/10.1130/0091-7613(1975)3<463:NATOMO>2.0.CO;2

Waldien, T. S., Roeske, S. M., Benowitz, J. A., Twelker, E., & Miller, M. S. (2021). Oligocene-Neogene lithospheric-scale reactivation of Mesozoic terrane accretionary structures in the Alaska Range suture zone, southern Alaska, USA. *GSA Bulletin*, *133*(3–4), 691–716. https://doi.org/10.1130/B35665.1

Wang, Y., Allam, A., & Lin, F. C. (2019). Imaging the fault damage zone of the san Jacinto fault near Anza with ambient noise tomography using a dense nodal array. *Geophysical Research Letters*, *46*(22), 12938–12948. https://doi.org/10.1029/2019GL084835

Wang, Y., Lin, F. C., & Ward, K. M. (2019). Ambient noise tomography across the Cascadia subduction zone using dense linear seismic arrays and double beamforming. *Geophysical Journal International*, *217*(3), 1668–1680. https://doi.org/10.1093/gji/ggz109

Wang, Y., & Tape, C. (2014). Seismic velocity structure and anisotropy of the Alaska subduction zone based on surface wave tomography. *Journal of Geophysical Research: Solid Earth*, *119*(12), 8845–8865. https://doi.org/10.1002/2014jb011438

Wang, Z., & Dahlen, F. A. (1995). Validity of surface-wave ray theory on a laterally heterogeneous earth. *Geophysical Journal International*, *123*(3), 757–773. https://doi.org/10.1111/j.1365-246X.1995.tb06888.x

Ward, K. M., & Lin, F. C. (2018). Lithospheric structure across the Alaskan cordillera from the joint inversion of surface waves and receiver functions. *Journal of Geophysical Research: Solid Earth*, *123*(10), 8780–8797. https://doi.org/10.1029/2018jb015967

Wells, D., Lin, F., Pankow, K., Baker, B., & Bartley, J. (2022). Combining dense seismic arrays and broadband data to image the subsurface velocity structure in geothermally active south-central Utah. *Journal of Geophysical Research: Solid Earth*, *127*(7), 1–23. https://doi.org/10.1029/2022jb024070

Wood, C. A., & Kienle, J. (1990). Volcanoes of north America: United States and Canada. In *Volcanoes of North America: United States and Canada* (1st edn.). Cambridge University Press. https://doi.org/10.1016/0031-9201(92)90173-s

Yang, X., & Gao, H. (2020). Segmentation of the Aleutian-Alaska subduction zone revealed by full-wave ambient noise tomography: Implications for the along-strike variation of volcanism. *Journal of Geophysical Research: Solid Earth*, *125*(11), e2020JB019677. https://doi.org/10.1029/2020JB019677

Yang, Y., & Ritzwoller, M. H. (2008). Characteristics of ambient seismic noise as a source for surface wave tomography. *Geochemistry, Geophysics, Geosystems*, *9*(2), Q02008. https://doi.org/10.1029/2007GC001814

Yao, H., Campman, X., de Hoop, M. V., & van der Hilst, R. D. (2009). Estimation of surface wave Green's functions from correlation of direct waves, coda waves, and ambient noise in SE Tibet. In *Physics of the Earth and planetary interiors, Issues 1–2* (Vol. 177, pp. 1–11). Elsevier BV. https://doi.org/10.1016/j.pepi.2009.07.002

CHAPTER 4

IMAGING VOLCANIC DIKE STRUCTURE IN THE EAST RIFT ZONE, HAWAII BIG ISLAND

Santiago Rabade[1], Fan-Chi Lin[1], Jamie Farrell[1], Sin-Mei Wu[2]

1. Department of Geology and Geophysics, University of Utah.
2. Lawrence Berkeley National Laboratory

Abstract

The 1840, 1955, and 2018 eruptions in the Lower East Rift Zone (LERZ) of Kilauea were followed and fed by different episodes of dike intrusions in the subsurface over 30 km away from the volcano summit reservoirs. To gain a better understanding of the dike emplacement and the magma transport process, we study the shallow crustal structure in the LERZ using a linear geophone nodal array deployed perpendicular to the dike. We use multi-component noise cross-correlations and beamforming/slant stacking methods to measure the phase velocity of Rayleigh and Love waves. Additionally, we calculated Rayleigh wave ellipticity using the larger island network. Colocated high-velocity anomalies of Love and Rayleigh wave phase velocities beneath the 1955 fissure, associated with a low velocity Love wave anomaly reveal the complexity of the shallow crustal structure.

1. Introduction

Moderate to large volcanic eruptions are infrequent but can cause widespread disruption of lives and extensive economic losses. About 800 million people live within 100 km of an active volcano (Freire et al., 2019). There are about 1,350 potentially active volcanoes worldwide, including 161 in the U.S., 18 of which are considered high threat and predominantly distributed in Alaska, California, Hawaii, Oregon, and Washington (Ewert et al., 2018). The hazards of volcanoes include lava flows, ash or tephra fall, ballistics, pyroclastic currents, debris flow or lahars, landslides, and ground shaking.

Lava flows are among the most common and destructive features of effusive volcanic eruptions, as anything impacted on its path is expected to be completely destroyed (Jenkins et al., 2017; Neal et al., 2019). In the case of Hawaii, lava flows typically traveled around 10–15 km from the eruptive vent; the longest flows observed have traveled up to 50 km (Malin, 1980). The magmatic material can also be transported in the subsurface from the storage near the volcanic edifice or caldera to the eruptive vents dozens of kilometers via dikes. Recent examples include the ~40 km long Bárdarbunga dike in 2015 (Gudmundsson et al., 2016), or the ~50 km long dike structure of Kilauea volcano in 2018 (Neal et al., 2019).

There are surface records of lava flows in the LERZ as old as 3000 y.o. (Sherod et al., 2021). Since 1950, the Hawaiian volcanic activity can be described as frequent with prolonged eruptions on the Kilauea crater and in the Kilauea East Rift Zone (ERZ). In 1955, there was a weeks-long eruption on the LERZ. From 1969 to 1974, eruptive activity occurred on the Mauna Ulu part of the Upper ERZ (UERZ) (Swanson et al., 1979; Tilling, 1987). From 1983 to the beginning of 2018, the activity centered on Puʻu ʻŌʻō located on the Middle ERZ (Parfitt and Wilson, 1994; Poland et al., 2014), and since 2006, from the Halemaʻumaʻu crater at the summit (Neal et al., 2019). The Southwest Rift Zone activity of Kilauea is limited to the 1971 and 1974 eruptions (Lockwood et al., 1999; Poland et al., 2014). Meanwhile, events on Mauna Loa have been restricted to two short-lived eruptions in July 1975 and March-April 1984 (Tilling et al., 2010).

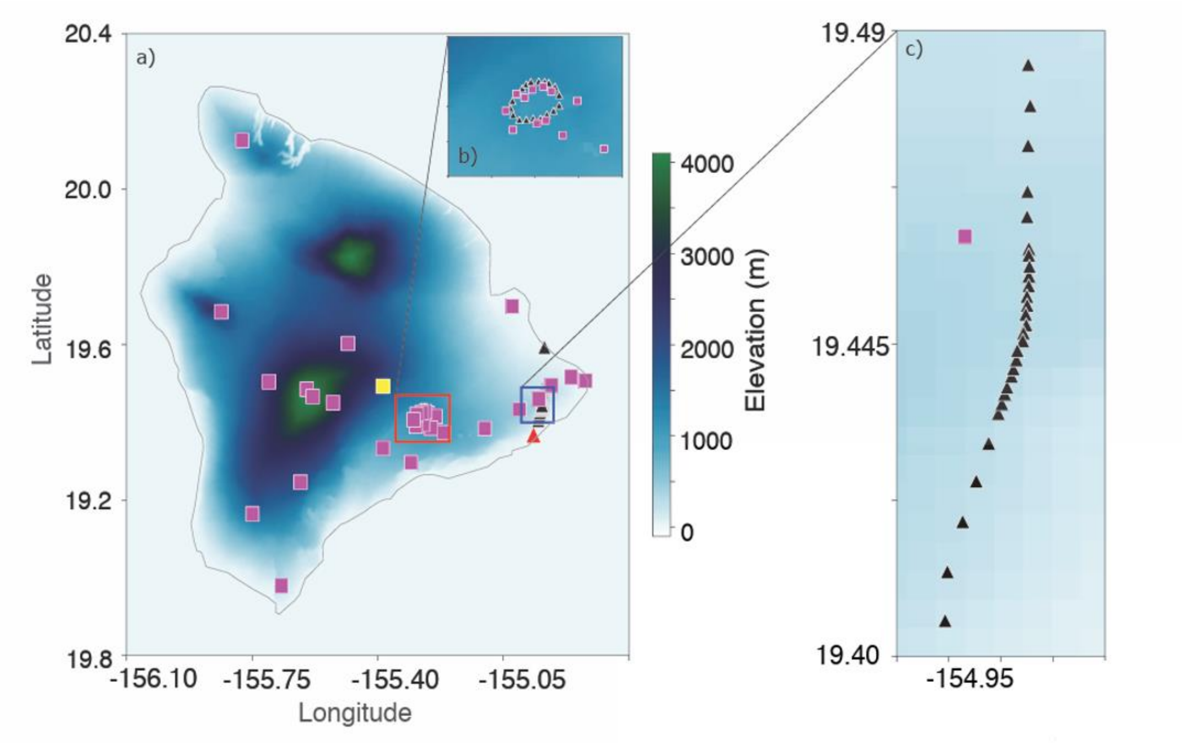

Figure 1. The magenta squares are the broadband stations, the yellow square is the virtual source for Figure 3a, and b. The black triangles are the temporal nodal array. The red triangle is the virtual source for Figure 2a, and b. a) Topographic map of Hawaii Big Island. b) Zoom in to the Kilauea summit. c) Zoom in to the linear nodal array.

In mid-March 2018, a net increase in magma supply caused inflation and the rise of the lava lake level in both cones, a good proxy of the increased pressurization on the system (Patrick et al., 2015). In the framework before the 2018 eruption, this kind of event would have caused a new discharge on Puʻu ʻŌʻō or its surroundings (Neal et al., 2019; M.R. Patrick et al., 2020). A decrease in the transport efficiency in the Puʻu ʻŌʻō cone has been hypothesized as the reason for the increase in pressurization (Patrick et al., 2020). On April 30, a new vent formed around Puʻu'Ōʻō, the floor of the crater collapsed, and the seismicity and the magmatic material started to move downrift towards the LERZ. The lava lake withdrawal began on May 1, and the first eruptive vent on the LERZ opened on May 3, extruding material with a similar composition to the 1955 eruption (Neal et al., 2019).

The collapse of the caldera at the summit and the effusive events downrift at the LERZ has been likened to a piston-like drop system. The collapse of the caldera floor serves as a piston that increases the pressure and the ERZ dike acts as the hydraulic connection between the summit and the LERZ (Patrick et al., 2019). The collapses were driven by the magma withdrawal from the summit reservoir (Neal et al., 2019). This pattern had also been noted in the Bárdarbunga and Fernandina caldera collapse. However, it is worth noting that there is no report of increased piston-like pressure for the 2007 collapse of Piton de la Fournaise (Gudmundsson et al., 2016). This piston-like system, added to the low elevation of the LERZ vent, made the 2018 eruption one of the largest in recorded history. In 4 months of effusive activity, the system extruded around 1 km3 (Neal et al., 2019; Patrick et al., 2020).

Improving our knowledge of underground magma transport is crucial by studying the velocity structure of active dikes to diminish the hazard associated with lava flows and magma transfer. Measuring the size of a dike is difficult (Rivalta et al., 2015). The GPS and/or InSAR-derived crustal deformation usually lacks resolution. During episodes of magmatic/dike intrusions, seismicity is abundant. However, the spatial distribution of seismicity is not solely associated with the dike propagation. Indirect modeling measurements usually have hard-to-constrain variables like dike section lengths, heights, widths, magma temperature, pressurization, and gas content. Passive and active seismic interferometry has proved to be a valuable and flexible tool to map the shallow crust, including small structures like fault zones (Mordret et al., 2019; Wang, Allam et al., 2019; Gkogkas et al., 2021, Rabade et al., 2023), as well as complex hydrothermal features (Wu et al., 2017, 2019, 2021). To better understand the transport of magma and the hydraulic connection between different features of the Kilauea volcano, we imaged the Lower East Rift Zone (LERZ) using Love and Rayleigh phase velocities measured from ambient cross-correlations of a temporal nodal array deployed in the spring of 2019.

2. Data and Methodology

2.1 Data

This study used ambient noise data from a semi-linear temporal deployment installed along Hawaii Route 130 (Figure 1b). The highway is located ~2 km west or uprift from fissure 8, the most effusive during the 2018 eruption. The temporal array consisted of 29 three-component 5 Hz nodal stations deployed from mid-March to late April 2019 with variable interstation distance. The main segment of the array is 27 stations with an end-to-end distance of ~10 km, formed by sparser edges and a central denser coverage above the presumed dike location with an interstation distance of ~200m. We also employed temporal stations deployed around the Kilauea caldera and permanent from the Hawaiian Volcano Observatory (add ref), the Pacific Tsunami Warning Seismic System (add ref), and the Global Seismograph Network (add ref).

2.2 Ambient Noise Cross-Correlation

We used the month-long noise recordings to calculate the 9-component noise cross-correlation following (Lin et al., 2014; Wu et al., 2017). To prepare the data, we pre-filter the signal between 0.1 and 50 s period, decimate the data to 50 samples per second, and cut the data into 5-minute segments. Then, for each nonoverlapping 5-minute segment, we calculate the cross-correlation using two different normalization processes. The first normalization process uses data from the entire array (Wu et al., 2020). The whitening is computed using the 90th percentile averaged three-component spectrum across the array for spectral normalization. For temporal normalization, we normalized by the 90th percentile maximum amplitude of the vertical–vertical CCFs across the entire array (Figure 2). For the second normalization process, we whiten the three-component data based on the vertical spectrum, and likewise, we do a temporal normalization by the maximum amplitude of the vertical (Wu et al., 2017) (Figure 3). The cross-correlations obtained with the whole array normalization are used to measure the phase velocity, and the cross-correlations obtained using the normalization by the vertical component are used for the Rayleigh wave ellipticity measurements.

2.3 Rayleigh and Love Wave Phase Velocity

Given that the array is sparser at the edges and denser at the center (Figure 1b), we use slant stacking or single beamforming (Rabade et al.,2023; Wang et al., 2019) (Figure 4) to measure Rayleigh and Love Wave phase velocity. This approach can enhance the signal and simultaneously measure local phase velocity. To create the beams, we use the station location as a beam center, and then we find the 7-closest stations, to be included in the beam, each station needs to pass two criteria: first, it needs to be one wavelength away from the source, and second, the station needs to be closer than 1.5 wavelengths from the receiver beam center, using a reference velocity of 1km/s. This approach results in variable beam size, larger at the edges and smaller at the middle of the array. We use the vertical-vertical (ZZ) cross-correlation for Rayleigh waves, and for Love waves, we use the transverse-transverse (TT) component. The phase velocity computation uses the same parameters for the two waveforms. First, we cut the signal to a reference velocity of 1km/s to remove earlier spurious arrivals (Wang et al., 2019, Gkogkas et al., 2021), and we taper and normalize the signal by its maximum amplitude. Then, we perform a coarse and fine grid search and shift and stack the waveforms to find the best phase slowness that maximizes the envelope amplitude. We stack the envelope amplitude at the maximum time for each source-receiver pair with a signal-to-noise ratio larger than 10. The maximum of the stack is the resulting phase velocity, and we defined the uncertainty as any value larger than 0.95 normalized amplitude.

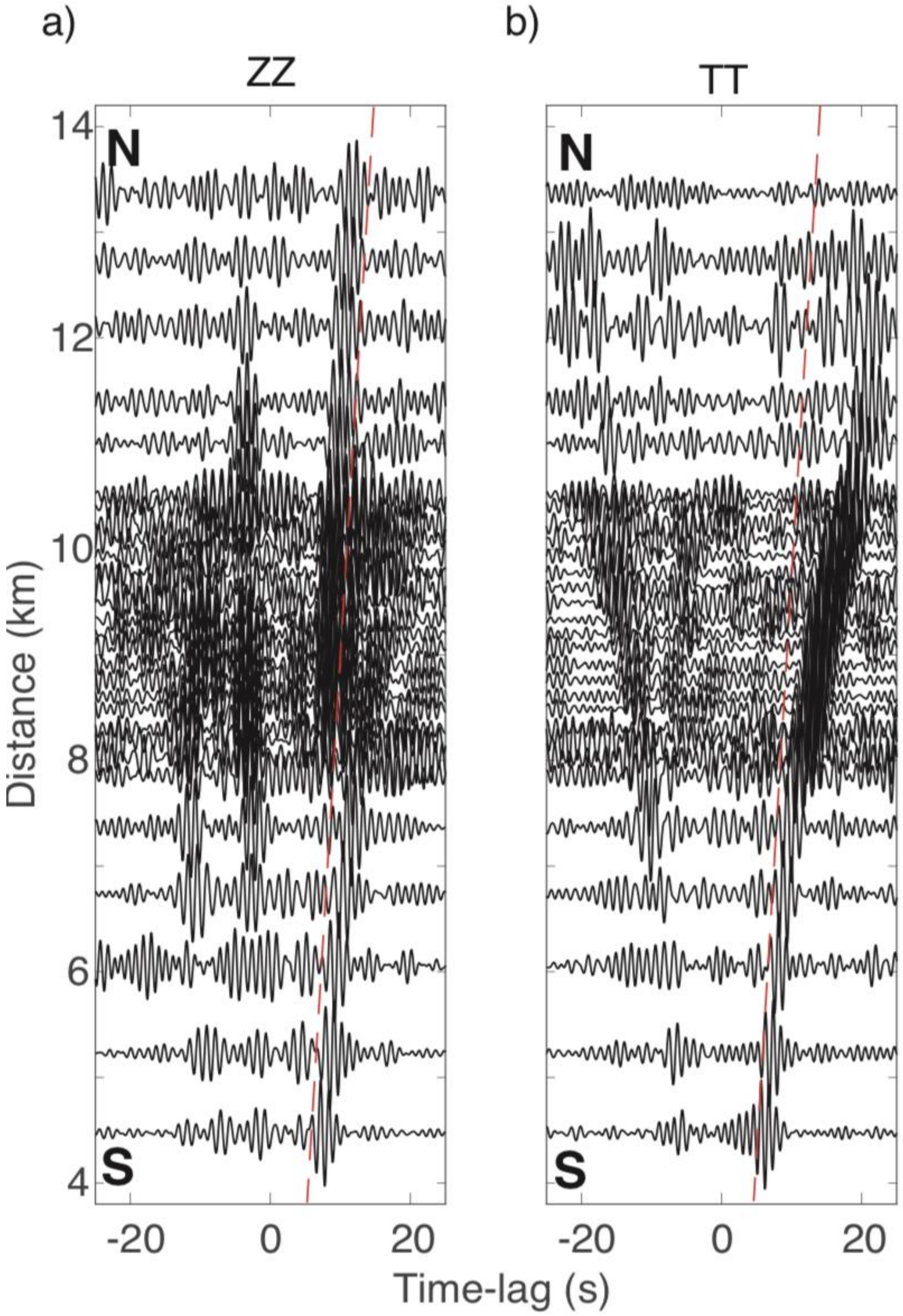

Figure 2. Example of noise cross-correlation record sections for the linear array calculated between the southernmost nodal station and all the receivers filtered around 1 s, reference dashed line 1km/s (a) ZZ, and b) TT.

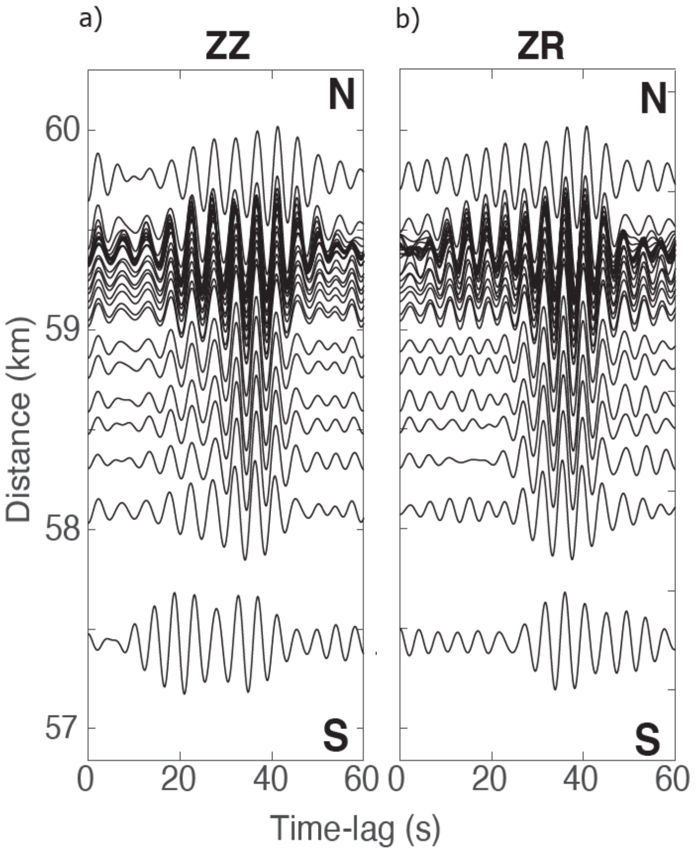

Figure 3. Example of symmetric noise cross-correlation record sections from a broadband station to the linear array around 5 s (a)ZZ, and (b) ZR.

2.3 Rayleigh Wave Ellipticity

Using the cross-correlation from the rest of the island to the linear array, we measure the Rayleigh wave ellipticity or horizontal-to-vertical (H/V) amplitude ratio. The H/V ratio is sensitive to velocity contrast directly beneath the station. For the H/V processing, we use the symmetric ZZ and vertical-radial (ZR) components of the cross-correlation (Figure 5). First, we obtain the group and phase travel time from frequency-time analysis (Bensen et al., 2007; Lin et al., 2008). Then, to measure the H/V, we use the envelope peak for each period (Berg et al., 2018, 2019; Lin et al., 2012) on waveforms passing two different criteria: first, an SNR larger than 5, and second, the phase travel time of the horizontal component should be within one-sixth of a period of the expected 90-degree phase shift (one-fourth of a period) between the vertical and radial components. We only use the common sources for all receivers to avoid any bias in the result from having a different number of measurements.

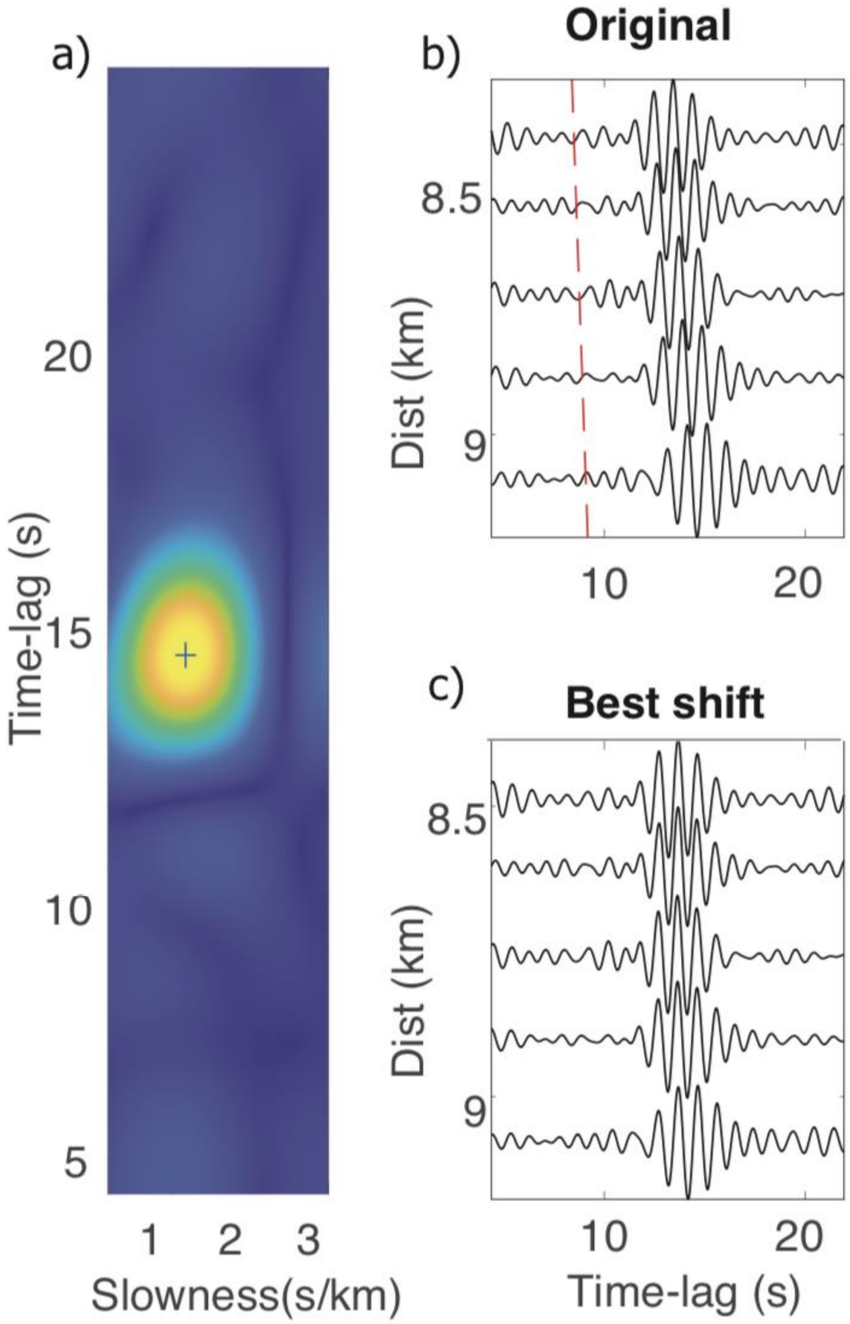

Figure 4. Example calculation of phase slowness based on slant stacking. (a) Amplitude as a function of time and phase slowness, the cross denotes the location of the maximum amplitude. (b) ZZ. (c) ZZ shifted by the maximum amplitude slowness. Reference dashed line 1km/s.

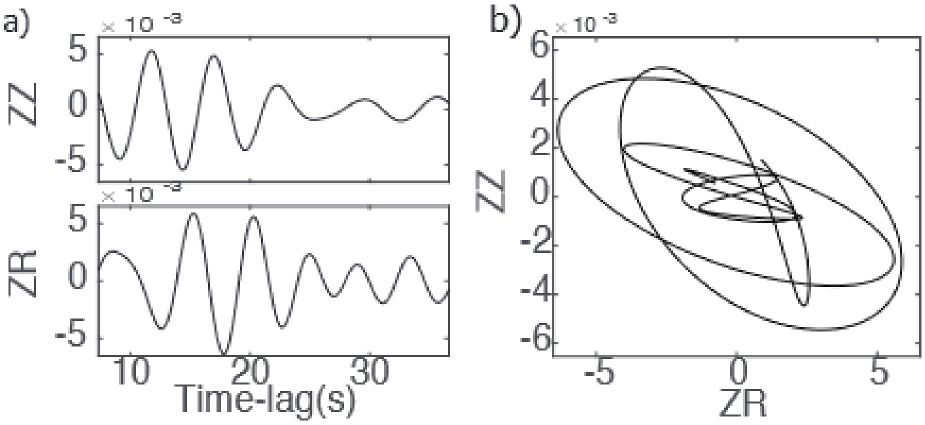

Figure 5. a) Cross-correlation function of components ZZ and ZR of station pair with virtual source on the Kilauea summit and receiver in the rift zone). b) Retrograde particle motion.

3. Results

3.1 Rayleigh and Love Wave Phase Velocity

The Rayleigh wave velocity result (Figure 6b) shows lower phase velocities on the southern end of the array and larger velocities on the northern section of the array. There is a continuous velocity increase from the south, with the maximum around ~200 m south of the dike. This high-velocity anomaly is around 1 km long. The velocity is constant north of the dike, with a subtle increase 900 m north of the dike.

The Love wave phase velocity for a 1-second period (Figure 6a) shows slightly larger velocities in the southern edge of the array than in the north. Around ~400 m south of the dike, there is also a 500m wide high-velocity anomaly, mostly colocated with the high-velocity Rayleigh wave anomaly. From 500 m to 1500 m north of the dike location, there is a low-velocity area of Love wave.

3.2 Rayleigh Wave Ellipticity

The resulting H/V ratio (Figure 7) shows a trend of larger ellipticity south of the dike location and lower ellipticity north of the dike location. In the deeper results (7 sec), the difference between the north and the south is larger than in the shallower result (5 sec). For these results, there is no clear anomaly regarding the dike signature.

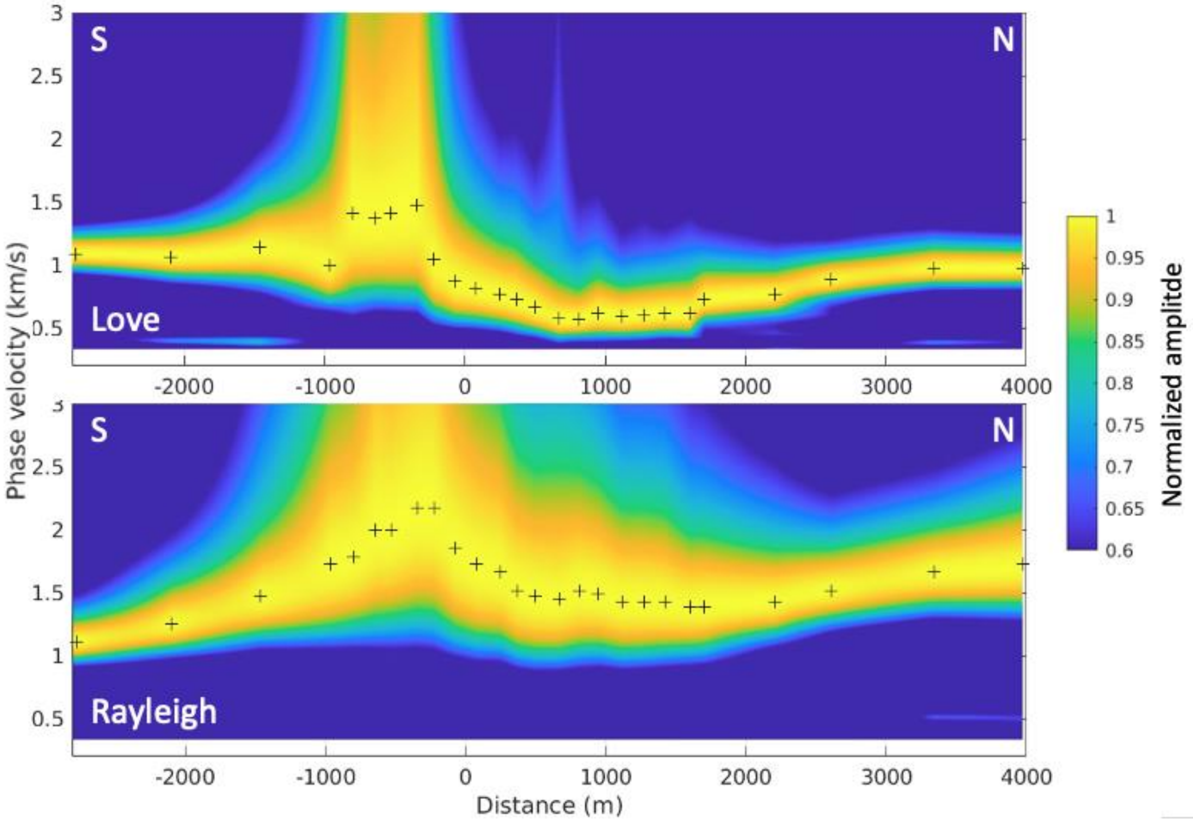

Figure 6. Phase Velocity profile for 1 second: a) Love wave, b) Rayleigh wave. The distance in the x-axis is calculated from the presumed dike location.

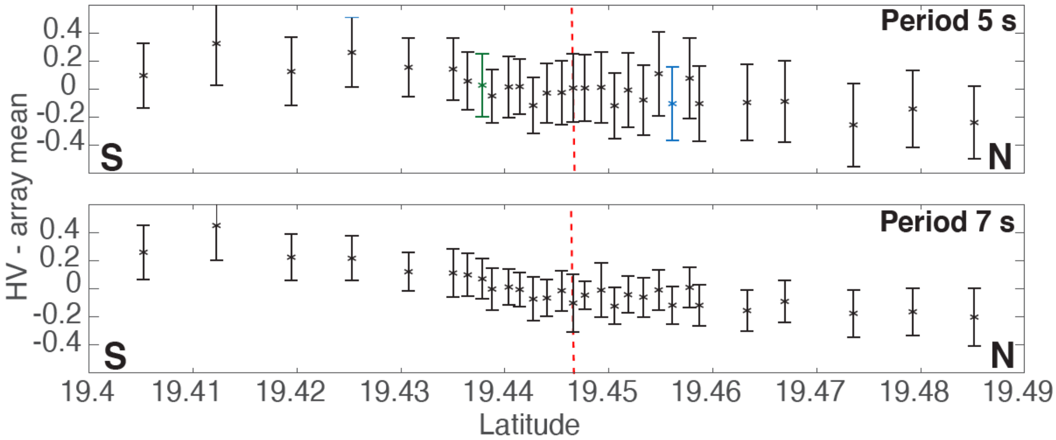

Figure 7. H/V results for periods 5 and 7 seconds.

4. Discussion

4.1 The dike

The colocated high-velocity anomalies of Love and Rayleigh wave phase velocity (Figure 6) can be related to the younger magmatic emplacements from the LERZ, previous observation suggest higher velocities in the LERZ (Wei et al., 2023; Lin et al., 2014). The anomaly is located beneath the relatively young 1955 LERZ eruption flows. This process is analogous to the high-velocity anomaly observed surrounding the magmatic chamber in volcanic settings (Paulato et al., 2022). The high-velocity area agrees with a low resistivity in the shallow, ~300m, and high resistivity at ~800m anomaly obtained from a 2013 survey (Warren et al., 2023).

Our result does not provide enough information to suggest any relation between this high-velocity anomaly and the 2018 eruption. We can hypothesize several scenarios. The first scenario is that the 2018 dike, with an estimated weight of ~20-30 m (Roman and Lundgren, 2023), and the resulting thermal anomaly are small, and the surface waves can not map them. The second scenario is that the signature of the high-velocity anomaly is larger than the signature of the 2018 dike, and the anomaly is a complex boundary that changes the shape and size of the surface waves, muting any signature of the ~20-30 m wide structure. The third scenario is that the high-velocity anomaly is the signal of the 2018 eruption. This hypothesis is supported by the fact that the initial lavas of the 2018 eruption had a composition similar to the 1955 lava (Neal et al., 2019). The other information is the different strikes between the fissures in 1840 and 1955 with the 2018 eruption. Projecting east, lines following the fissures of 2018 and the fissures of 2018 intersect ~2 km east of the array. It is unclear if the material was following the same trace as 1955 and locally diverged to use a different set of cracks to reach the surface. We do not observe an anomaly related to the 1840 eruption in the northern section of the array.

We interpret the low Love wave velocity anomaly as a highly fracture media product of the different dike intrusions and the normal faulting related to the island decollement (Clague and Sherrod, 2014; Denlinger and Morgan, 2014). Our measurements suggest that the LERZ width is 3.5 to 4 km.

4.2 Larger Scale Tectonic Structure

The larger scale tectonic structure from phase velocity (Figure 6) and ellipticity (Figure 7) suggests that in the southern part of the array, the crust is more homogeneous with similar velocity for shallower sensitivity Love waves and deeper sensitivity Rayleigh waves. The higher H/V in that area suggests a velocity contrast deeper than the sensitivity of the phase velocity. In the northern edge of the array, there are differences in velocity between Rayleigh and Love waves, and the smaller H/V suggests there is no velocity contrast at depth. We infer that the velocity differences between the deeper velocity contrast in the south and the shallower velocity contrast in the north are related to the differences in the emplacement type of the basaltic lavas of the Kilauea system. In the shallow, the crust is dominated by lava flows, and at depth is dominated by lava pillows from submarine eruptions. Our result points to a thicker lava flow in the south and thinner lava flows in the north. This large scale pattern is consistent with peak-ground-velocity measured at the same locations during 2018 eruptions (Wu et al., 2020) and with island-wide tomography (Wei et al., 2023)

5. Conclusions

In conclusion, our analysis reveals insights into the geological dynamics of the LERZ Kilauea Volcano region. The presence of colocated high-velocity anomalies in Love and

Rayleigh wave phase velocities beneath the younger magmatic emplacements from the LERZ suggests a complex interplay between volcanic activity and crustal structure. While our findings do not definitively link the observed high-velocity anomaly to the 2018 eruption, several scenarios are proposed, highlighting the need for further investigation. Additionally, the interpretation of a low Love wave velocity anomaly as a product of highly fractured media underscores the intricate nature of dike intrusions and faulting in the area. Furthermore, the broader tectonic implications discussed by the differences in crustal velocity structures between the southern and northern edges of the array shed light on the emplacement patterns of basaltic lavas within the Kilauea system. These findings contribute to a deeper understanding of the geological processes at play in this dynamic volcanic region and underscore the importance of continued research efforts to discover its complexities.

6. References

Bensen, G.D., Ritzwoller, M.H., Barmin, M.P., Levshin, A.L., Lin, F., Moschetti, M.P., Shapiro, N.M. and Yang, Y., 2007. Processing seismic ambient noise data to obtain reliable broad-band surface wave dispersion measurements. Geophysical journal international, 169(3), pp.1239-1260.

Berg, E.M., Lin, F.C., Allam, A., Qiu, H., Shen, W. and Ben-Zion, Y., 2018. Tomography of Southern California via Bayesian joint inversion of Rayleigh wave ellipticity and phase velocity from ambient noise cross-correlations. Journal of Geophysical Research: Solid Earth, 123(11), pp.9933-9949.

Berg, E.M., Lin, F.C., Allam, A., Schulte-Pelkum, V., Ward, K.M. and Shen, W., 2020. Shear velocity model of Alaska via joint inversion of Rayleigh wave ellipticity, phase velocities, and receiver functions across the Alaska Transportable Array. Journal of Geophysical Research: Solid Earth, 125(2), p.e2019JB018582.

Clague, D. A., and D. R. Sherrod, 2014, Growth and degradation of Hawaiian volcanoes, Reston, VA.

Denlinger, R. P., and J. K. Morgan, 2014, Instability of Hawaiian volcanoes, Reston, VA.

Freire, S., A. J. Florczyk, M. Pesaresi, and R. Sliuzas, 2019, An improved global analysis of population distribution in proximity to active volcanoes, 1975-2015, ISPRS Int. J. Geo-Information, 8, no. 8, doi: 10.3390/ijgi8080341.

Gkogkas, K., F. C. Lin, A. A. Allam, and Y. Wang, 2021, Shallow damage zone structure of the wasatch fault in Salt Lake City from ambient-noise double beamforming with a temporary linear array, Seismol. Res. Lett., 92, no. 4, 2453–2463, doi: 10.1785/0220200404.

Gudmundsson, M. T. et al., 2016, Gradual caldera collapse at Bárdarbunga volcano, Iceland, regulated by lateral magma outflow, Science (80-.)., 353, no. 6296, doi: 10.1126/science.aaf8988.

Jenkins, S. F., S. J. Day, B. V. E. Faria, and J. F. B. D. Fonseca, 2017, Damage from lava flows: insights from the 2014–2015 eruption of Fogo, Cape Verde, J. Appl. Volcanol., 6, no. 1, doi: 10.1186/s13617-017-0057-6.

Lin, F.C., Moschetti, M.P. and Ritzwoller, M.H., 2008. Surface wave tomography of the western United States from ambient seismic noise: Rayleigh and Love wave phase velocity maps. Geophysical Journal International, 173(1), pp.281-298.

Lin, F.C., Tsai, V.C. and Schmandt, B., 2014. 3-D crustal structure of the western United States: application of Rayleigh-wave ellipticity extracted from noise cross-correlations. Geophysical Journal International, 198(2), pp.656-670

Lin, G., Shearer, P.M., Matoza, R.S., Okubo, P.G. and Amelung, F., 2014. Three-dimensional seismic velocity structure of Mauna Loa and Kilauea volcanoes in Hawaii from local seismic tomography. *Journal of Geophysical Research: Solid Earth*, *119*(5), pp.4377-4392.

Lockwood, J. P., R. I. Tilling, R. T. Holcomb, F. W. Klein, A. T. Okamura, and D. W. Peterson, 1999, Magma migration and resupply during the 1974 summit eruptions of Kilauea Volcano, Hawaii.

Malin, M. C., 1980, Lengths of Hawaiian lava flows, Geology, 8, no. 7, 306, doi: 10.1130/0091-7613(1980)8<306:LOHLF>2.0.CO;2.

Mordret, A., P. Roux, P. Boué, and Y. Ben-Zion, 2019, Shallow three-dimensional structure of the San Jacinto fault zone revealed from ambient noise imaging with a dense seismic array, Geophys. J. Int., 216, no. 2, 896–905, doi: 10.1093/gji/ggy464.

Neal, C. A. et al., 2019, The 2018 rift eruption and summit collapse of Kīlauea Volcano, Science (80-.)., 363, no. 6425, 367–374, doi: 10.1126/science.aav7046.

Parfitt, E. A., and L. Wilson, 1994, The 1983-86 Pu'u 'O'o eruption of Kilauea Volcano, Hawaii: a study of dike geometry and eruption mechanisms for a long-lived eruption, J. Volcanol. Geotherm. Res., 59, no. 3, 179–205, doi: 10.1016/0377-0273(94)90090-6.

Patrick, M. R., K. R. Anderson, M. P. Poland, T. R. Orr, and D. A. Swanson, 2015, Lava lake level as a gauge of magma reservoir pressure and eruptive hazard, Geology, 43, no. 9, 831–834, doi: 10.1130/G36896.1.

Patrick, M. R., H. R. Dietterich, J. J. Lyons, A. K. Diefenbach, C. Parcheta, K. R. Anderson, A. Namiki, I. Sumita, B. Shiro, and J. P. Kauahikaua, 2019, Cyclic lava effusion during the 2018 eruption of Kīlauea Volcano, Science (80-.)., 366, no. 6470, doi: 10.1126/science.aay9070.

Patrick, M. R., B. F. Houghton, K. R. Anderson, M. P. Poland, E. Montgomery-Brown, I. Johanson, W. Thelen, and T. Elias, 2020, The cascading origin of the 2018 Kīlauea eruption and implications for future forecasting, Nat. Commun., 11, no. 1, 5646, doi: 10.1038/s41467-020-19190-1.

Patrick, M., I. Johanson, T. Shea, and G. Waite, 2020, The historic events at Kīlauea Volcano in 2018: summit collapse, rift zone eruption, and Mw 6.9 earthquake: preface to the special issue, Bull. Volcanol., 82, no. 6, 2018–2021, doi: 10.1007/s00445-020-01377-5.

Patrick, M., T. Orr, K. Anderson, and D. Swanson, 2019, Eruptions in sync: Improved constraints on Kīlauea Volcano's hydraulic connection, Earth Planet. Sci. Lett., 507, 50–61, doi: 10.1016/j.epsl.2018.11.030.

Paulatto, M., Hooft, E.E., Chrapkiewicz, K., Heath, B., Toomey, D.R. and Morgan, J.V., 2022. Advances in seismic imaging of magma and crystal mush. *Frontiers in Earth Science*, *10*, p.970131.

Poland, M. P., A. Miklius, and E. K. Montgomery-Brown, 2014, Magma supply, storage, and transport at shield-stage Hawaiian volcanoes, Reston, VA.

Rabade, S., Lin, F.C., Tape, C., Ward, K.M., Waldien, T. and Allam, A., 2023. The crustal magmatic structure beneath the Denali Volcanic Gap imaged by a dense linear seismic array. Journal of Geophysical Research: Solid Earth, 128(12), p.e2023JB027152.

Roman, A. and Lundgren, P., 2023. Magma Transport and Storage Along Rift Zones Through Volcanic Conduits. Journal of Geophysical Research: Solid Earth, 128(8), p.e2023JB026509.

Rivalta, E., B. Taisne, A. P. Bunger, and R. F. Katz, 2015, A review of mechanical models of dike propagation: Schools of thought, results and future directions, Tectonophysics, 638, no. C, 1–42, doi: 10.1016/j.tecto.2014.10.003.

Sherrod, D.R., Sinton, J.M., Watkins, S.E. and Brunt, K.M., 2021. Geologic map of the State of Hawaii (No. 3143). US Geological Survey.

Swanson, D. A., W. A. Duffield, D. B. Jackson, and D. W. Peterson, 1979, Chronological narrative of the 1969-71 Mauna Ulu eruption of Kilauea Volcano, Hawaii, U.S. Geol. Surv. Prof. Pap. 1056, 1056, 55 p.

Tilling, R. I., 1987, The 1972-1974 Mauna Ulu eruption, Kilauea Volcano: an example of quasi-steady-state magma transfer (Hawaii)., US Geol. Surv. Prof. Pap., 1350, no. 1, 405–469.

Tilling, R. I., C. Heliker, and D. A. Swanson, 2010, Eruptions of Hawaiian volcanoes; past, present, and future, U.S. Geol. Surv. Gen. Inf. Prod. 117, 1–72.

Wang, Y., A. Allam, and F. C. Lin, 2019, Imaging the Fault Damage Zone of the San Jacinto Fault Near Anza With Ambient Noise Tomography Using a Dense Nodal Array, Geophys. Res. Lett., 46, no. 22, 12938–12948, doi: 10.1029/2019GL084835.

Wang, Y., F. C. Lin, and K. M. Ward, 2019, Ambient noise tomography across the Cascadia subduction zone using dense linear seismic arrays and double beamforming, Geophys. J. Int., 217, no. 3, 1668–1680, doi: 10.1093/gji/ggz109.

Warren, I., Friedel, M.J., Wallin, E., Lautze, N., Hou, Z.J., Vasco, D.W., Glubokovskikh, S., Gritto, R., Jarpe, S., Martel, S.J. and Jaysaval, P., 2023. *Innovative Subsurface Learning and Hawaiian Exploration using Advanced Tomography (ISLAND HEAT) Phase 1 Final Report* (No. NREL/TP-5700-87316). National Renewable Energy Laboratory (NREL), Golden, CO (United States).

Wei, X., Shen, Y. and Morgan, J.K., 2023. Shallow volcano-tectonic structures on the Island of Hawai ʻi imaged by multimode Rayleigh wave ambient noise tomography. *Journal of Geophysical Research: Solid Earth*, p.e2022JB026244.

Wu, S. M., F. C. Lin, J. Farrell, and A. Allam, 2019, Imaging the Deep Subsurface Plumbing of Old Faithful Geyser From Low-Frequency Hydrothermal Tremor Migration, Geophys. Res. Lett., 46, no. 13, 7315–7322, doi: 10.1029/2018GL081771.

Wu, S. M., F. C. Lin, J. Farrell, W. E. Keller, E. B. White, and J. D. G. Hungerford, 2021, Imaging the Subsurface Plumbing Complex of Steamboat Geyser and Cistern Spring With Hydrothermal Tremor Migration Using Seismic Interferometry, J. Geophys. Res. Solid Earth, 126, no. 4, doi: 10.1029/2020JB021128.

Wu, S. M., F. C. Lin, J. Farrell, B. Shiro, L. Karlstrom, P. Okubo, and K. Koper, 2020, Spatiotemporal Seismic Structure Variations Associated With the 2018 Kīlauea Eruption Based on Temporary Dense Geophone Arrays, Geophys. Res. Lett., 47, no. 9, 1–10, doi: 10.1029/2019GL086668.

Wu, S. M., K. M. Ward, J. Farrell, F. C. Lin, M. Karplus, and R. B. Smith, 2017, Anatomy of Old Faithful From Subsurface Seismic Imaging of the Yellowstone Upper Geyser Basin, Geophys. Res. Lett., 44, no. 20, 10,240-10,247, doi: 10.1002/2017GL075255.

CHAPTER 5

CONCLUSIONS

In this dissertation, I presented three projects detailing how more information regarding the crustal structure or the temporal variations of seismic signals can help to understand the geohazards of natural and human-made systems. Combining ambient noise interferometry to enhance signals and cheap and reliable nodal seismic stations can be a cost-effective strategy to reduce risk.

For Alaska, we obtained a shear wave velocity model of the top 16 km by jointly inverting Rayleigh wave phase velocity and ellipticity from ambient noise cross-correlations. We observed a low-velocity anomaly beneath the Denali Volcanic Gap, which we interpret as subduction-related magmatic material. We also observed the Denali Fault as a sharp, narrow, low-velocity anomaly extending to a depth of 12 km. We interpret the Hines Creek Fault trace as the northern limit of the Alaska Suture Zone. These three main observations shed light on the far-field effects of subduction zones, the evolution of arc volcanism in flat slab subductions and the Cordilleran strike-slip systems. Methodologically, we propose to use phase shift between Rayleigh waves in the ZZ and ZR components as a quality control criterion to remove spurious Rayleigh wave measurements.

For Hawaii, we use Rayleigh and Love phase wave velocity and Rayleigh wave ellipticity to analyze the shallow structure of the Lower East Rift Zone of the Kilauea volcano system. Within the rift zone, we measure larger velocities south of the presumed dike location and lower velocities north of the dike. In the larger scale structure, farther from the dike, we observe larger velocities north and a similar velocity structure in the shallow. The shallow to deep pattern can be related to the emplacement method of the basalts, from lava flows to lava pillows.

For the Longwall coal mine, we developed a workflow to extract and separate the signals generated from mining activity from the background seismic noise of the area. Then, we located the mine signals using the entire waveform at short- and long-time scales. These workflows can be used to monitor real-time seismic sources in many active environments, for example, mines, volcanoes, geothermal or hydrothermal systems, fracking or wastewater injection sites, or oil and gas extraction areas. This study underscores the potential of seismic noise analysis as a robust tool for real-time monitoring of seismic sources in active industrial settings, with implications for enhancing hazard assessment and risk management practices in mining operations.